# Zero electron kinetic energy and threshold photodetachment spectroscopy of $Xe_nI^-$ clusters ($n=2-14$): Binding, many-body effects, and structures

Thomas Lenzer,[a] Michael R. Furlanetto,[b] Nicholas L. Pivonka, and Daniel M. Neumark[c]
*Department of Chemistry, University of California, Berkeley, California 94720, and Chemical Sciences Division, Lawrence Berkeley National Laboratory, Berkeley, California 94720*

(Received 13 November 1998; accepted 12 January 1999)

$Xe_nI^-$ van der Waals clusters have been investigated by anion zero electron kinetic energy (ZEKE) and partially discriminated threshold photodetachment (PDTP) spectroscopy. The experiments yield size-dependent electron affinities (EAs) and electronic state splittings between the X, I, and II states accessed by photodetachment. Cluster minimum energy structures have been determined by extensive simulated annealing molecular dynamics calculations using $Xe–I^{(-)}$ pair potentials from anion ZEKE spectroscopy and various nonadditive terms. The EAs calculated without many-body effects overestimate the experimental EAs by up to 3000 $cm^{-1}$. Repulsive many-body induction in the anion clusters is found to be the dominant nonadditive effect, though the attractive interaction between the iodide charge and the $Xe_2$ exchange quadrupole is also important. Unique global minimum energy structures for the anion clusters arise from the influence of the many-body terms, yielding, e.g., arrangements with a closed shell of xenon atoms around the iodide anion for the clusters with $n=12-14$. The specific dependence of the EA curve on cluster size allows us to refine the absolute Xe–I bond lengths for the anion, X, I, and II state diatomic potentials to within $\pm 0.05$ Å. © *1999 American Institute of Physics.* [S0021-9606(99)01014-4]

## I. INTRODUCTION

Weak interactions between atoms and molecules play a central role in many fields of physical chemistry. As an example, solvation of neutral or charged atomic and molecular species affects their photophysical properties and reactivity in solution,[1,2] matrices,[3] crystals,[4] and clusters.[5–8] In recent years we have conducted a series of experiments in which the weak interactions between various solvent species and halide ions/halogen atoms is probed by high resolution negative ion photodetachment spectroscopy of size-selected anions; the species of interest range in size from binary complexes to large clusters. Here, we report results for $Xe_nI^-$ clusters, with the goal of understanding the many-body effects that govern the structure and energetics of these species.

In the description of weak interactions, *pairwise additivity* of the atom–atom interactions $V_{ij}$ is frequently assumed:

$$V_p=\sum_{i<j}^{N} V_{ij}(|\mathbf{r}_i-\mathbf{r}_j|), \tag{1}$$

where $\mathbf{r}_i$ and $\mathbf{r}_j$ denote the positions of two individual atoms in an ensemble of $N$ particles. For closed valence shell atoms and without deformation of the atomic charge distributions, Eq. (1) would hold exactly. In reality, however, dispersion, induction, and exchange interactions cause the assumption of pairwise additivity to break down.[9] Therefore it is necessary to extend Eq. (1) to include ''*nonadditive*'' or ''*many-body*'' interactions:

$$V_{\text{many-body}}=\sum_{i<j<k}^{N} V_{ijk}(\mathbf{r}_i,\mathbf{r}_j,\mathbf{r}_k)+\cdots + \sum_{i<j<k<\cdots<z}^{N} V_{ijk\cdots z}(\mathbf{r}_i,\mathbf{r}_j,\mathbf{r}_k,\ldots,\mathbf{r}_z). \tag{2}$$

A textbook example of nonadditivity is the binding energy of rare gas crystals, where the experimental values are roughly 4%–9% smaller than those obtained from the precisely known pair potentials.[10] However, in bulk systems such as these it is difficult to assess the contributions of individual nonadditive effects.

High resolution spectroscopy of clusters provides another approach to nonadditive effects in systems with a small number of atoms.[10,11] For example, Fourier transform microwave spectroscopy has been used to study the rotational spectra of the rare gas heterotrimers $Ne_2Kr$ and $Ne_2Xe$.[12] Structural information and nuclear hyperfine coupling constants obtained from this study suggest the presence of nonadditive effects.

Near- and far-IR spectroscopic studies as well as calculations employing variationally adjusted or *ab initio* potential energy surfaces have been carried out for several neutral van der Waals clusters, including $Ar_2HCl$,[10,13–16] $Ar_2HF$,[14,15,17–21] $Ar_2DCl$,[10,22] and $Ar_2CO_2$.[23,24] Other experimental studies involved laser-induced fluorescence detection of $Ar_nBa$ clusters with an average size of 300–4000[25] and electronic spectroscopy of mass-selected $Ar_nHg$ clusters ($n$

[a]Deutsche Forschungsgemeinschaft Postdoctoral Fellow.
[b]National Science Foundation Predoctoral Fellow.
[c]Electronic mail: dan@radon.cchem.berkeley.edu

 

$=1-4$) by means of multiphoton ionization.[26] The latter study shed some light on the special class of ''nonadditive'' effects arising from the open-shell interactions of the chromophores in the excited electronic state of these clusters.

The measurement of binding energies opens up another avenue to characterize nonadditive effects in clusters. Binding energies have the advantage that they can be obtained from model many-body potentials in a straightforward way. It is often easy to predict in which direction a particular nonadditive term will change the binding energy of a cluster. For charged species, anion photoelectron spectroscopy (PES) has been used to extract information on *relative* binding energies of anion and neutral clusters involved in the photodetachment process, providing mass selectivity and reasonable spectral resolution. Examples include the studies of Cheshnovsky and co-workers on $X^-(H_2O)_n$ ($X^-=Cl^-, Br^-, I^-$)[27] and $Xe_nI^-$,[28,29] Bowen and co-workers on $Ar_nO^-$,[30] and Arnold *et al.* on $X^-(CO_2)_n$ ($X^-=Br^-, I^-$) and $I^-(N_2O)_n$.[31,32]

However, two problems arise when one tries to extract information on nonadditive forces from such studies: (1) the pair potentials needed for the anion and neutral are usually not known very accurately, and (2) depending on the type of energy analyzer used, the resolution of conventional anion PES is typically between 70[31–33] and 480 $cm^{-1}$.[28,29] Due to this limited resolution anion PES experiments are, at best, sensitive to the largest nonadditive effects. As an example, a comparison of the photoelectron spectra of Markovich *et al.*[27] with the molecular dynamics (MD) simulations of Berkowitz and co-workers,[34] showed that nonadditive induction effects had to be included in the calculations to describe the stabilization energies of larger $Br^-(H_2O)_n$ clusters ($n>5$) correctly. However, a comparison of their experimental data for $I^-(H_2O)_n$ and $Cl^-(H_2O)_n$ clusters with other simulations[35,36] is less conclusive.

In the current study we use anion zero electron kinetic energy (ZEKE) spectroscopy and partially discriminated threshold photodetachment (PDTP) to study nonadditive effects in size-selected $Xe_nI^-$ clusters with up to 14 xenon atoms. ZEKE spectroscopy combines mass selectivity with much higher resolution than conventional photoelectron spectroscopy (typically 1–2 $cm^{-1}$ for atomic systems). It is therefore possible to extract precise electron affinities (EAs) and characterize the electronic structure of the neutral clusters accessed by photodetachment. We have already demonstrated this in our earlier ZEKE studies of diatomic[33,37,38] and polyatomic[39] rare gas halides. The latter study on $Ar_nI^-$ ($n=2-19$) and $Ar_nBr^-$ ($n=2-9$) allowed us to characterize the many-body effects in these species in detail.

$Xe_nI^-$ clusters are particularly interesting systems. First, the high polarizability of the xenon atoms makes it likely that nonadditive effects will be particularly large, especially in the anions. This makes these clusters ideal candidates for the investigation of many-body effects. Another distinctive property of $Xe_nI^-$ clusters was demonstrated in recent work by Cheshnovsky and co-workers,[28,29] who measured photoelectron spectra and total photodetachment cross sections (TPCS) for $Xe_nI^-$ clusters with $n=1-54$. For clusters with $n\geqslant 4$, they observed distinct peaks in the TPCS spectra near the detachment thresholds that appear to be due to transitions

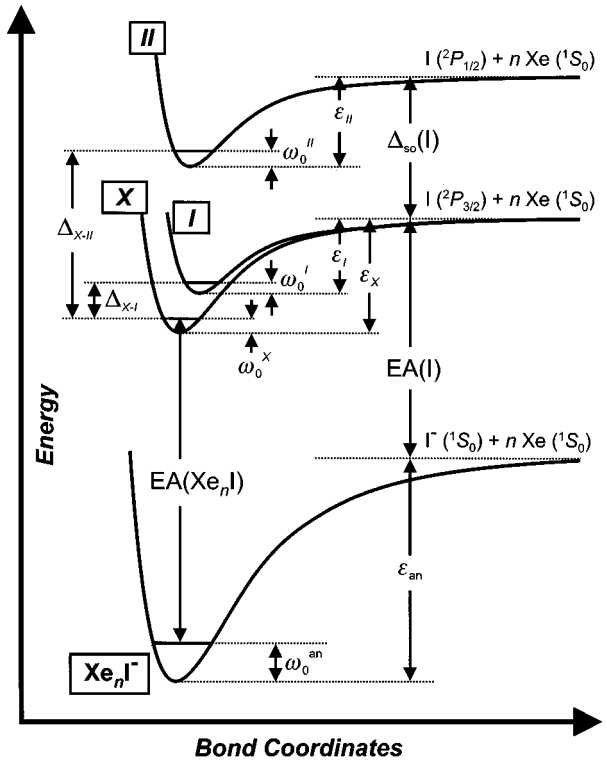


FIG. 1. Schematic diagram of the potential energy levels involved in the photodetachment of $Xe_nI^-$ clusters. The energetic relations among the atomic and molecular anion and neutral electronic states are shown. For a description of the various quantities see Sec. IV.

to excited electronic states in which charge is transferred from the iodide anion to the surrounding xenon atoms. These states, which presumably arise from the large polarizability of the xenon atoms, were not present in any of the rare gas–halide clusters previously studied by us.

Moreover, a unique class of ''nonadditive effects'' is present solely in the neutral clusters due to the open-shell nature of the iodine atom. Three doubly degenerate neutral electronic states (termed as X, I, and II) arise from this interaction, as shown in the schematic potential diagram in Fig. 1. All these states are accessible by photodetachment of the anion, and this allows us to characterize the splitting between the different neutral states as a function of cluster size.

Our earlier study of $XeI^-$ yielded precise two-body Xe–I anion and neutral potential functions via vibrationally resolved ZEKE spectroscopy.[33] This allows us to predict binding energies and structures of the larger anion and neutral $Xe_nI$ clusters on the basis of these pair potentials, and then to compare these predictions with the experimental EAs. It will become clear that the simple ''additive picture'' breaks down, so we will systematically investigate how the inclusion of various many-body effects corrects the calculated EAs and can finally achieve good agreement with experiment. Our accompanying MD simulations of the $Xe_nI$ anion and neutral cluster structures will not only help us to elucidate the cluster structures and trends in electron affinities but also allow us to determine the Xe–I equilibrium bond lengths for the anion and neutral electronic states of the diatomic with considerably higher accuracy.

We have organized this paper as follows: in Sec. II we

briefly discuss the experimental techniques used for studying the $Xe_nI^-$ anions, and in Sec. III our ZEKE and PDTP spectra are presented and assignments are given. In Sec. IV we deal with the two-body and three-body potential functions needed for simulating our results, and specifics of the MD calculations used for calculating the cluster structures are also given. In Sec. V we analyze and discuss our experimental findings: electron affinities and neutral state splittings are compared with the predictions of the model potentials and allow us to quantify the influence of individual many-body effects. Global and local minimum cluster structures found in the simulations are discussed in detail. We will finally address the question to what extent a presence of excited states in the larger anion clusters might affect the appearance of the experimental ZEKE and PDTP spectra.

## II. ZEKE AND PDTP EXPERIMENTS

A detailed description of the anion ZEKE spectrometer can be found elsewhere,[40–43] and only the specific details relevant to this study will be considered here. $Xe_nI^-$ anions are produced by passing a mixture of 10%–20% xenon in argon over $CH_3I$ (0 °C) and expanding it into vacuum through a 0.5 mm aperture in a pulsed valve (General Valve Series 9). Typical backing pressures are 10–30 psig. The expansion is crossed just in front of the valve by a 1 keV electron beam. Anions are formed by dissociative attachment of low-energy secondary electrons, and undergo clustering in the continuum flow region of the free-jet expansion. The negative cluster ions formed during these processes are cooled as the expansion progresses, and then pass through a two-skimmer setup[33] into a differentially pumped region. The clusters are then accelerated to 1 keV and mass selected in a 1 m collinear time-of-flight mass spectrometer.

After entering the detector region the $Xe_nI^-$ anions of interest are photodetached by either an excimer-pumped dye laser (Lambda Physik EMG 202 and FL 3002) or a Nd:YAG pumped dye laser (Continuum Powerlite 9020 and ND 6000). For photodetachment to the X and I states (see Fig. 1) several UV dyes are used (QUI, DMQ, PTP, all from Exciton) with typical energies of 20–30 mJ/pulse, except for the region below 336 nm, where a DCM/LDS698 mix is used in conjunction with frequency doubling in a KDP crystal, yielding about 5–10 mJ/pulse. For the II state the dye laser fundamental (Coumarin 540A, Rhodamine 590, 610, 640) is doubled in a KDP crystal, yielding laser pulse energies of 2–13 mJ/pulse, depending on the laser system used.

A weak DC field of −15 mV/cm is applied across the electron detachment region at all times, where the negative sign indicates the field is antiparallel to the ion beam propagation direction. This setup was found to enhance the electron signal considerably.[33] Two modes of electron detection were used in this study: the higher resolution ZEKE mode and the lower resolution partially discriminated threshold photodetachment (PDTP) mode.

In the ZEKE mode, following a delay of 200–500 ns the electrons are extracted coaxially to the ion beam by applying a pulsed extraction field of 4 V/cm across the extraction region and deflected to an off-axis microchannel plate detector. Gated detection is used to provide temporal filtering. In addition, a series of apertures between the detachment region and the detector provide spatial discrimination.[40] The ultimate spectral resolution of this setup is about 1–2 $cm^{-1}$ for atomic anions. The spectral features observed in this study are broader due to unresolved rotational envelopes and ''hot band'' congestion. Also, somewhat shorter extraction delays than required for maximum resolution were used, leading to a slight decrease in resolution but more rapid data acquisition. The performance of the ZEKE mode was routinely checked by optimizing the spectral resolution for the well-known systems $I^-$ and $XeI^-$.[33]

In the PDTP mode there is no delay between photodetachment and electron extraction. The extraction field immediately accelerates all of the photoelectrons toward the detector. However, those photoelectrons with a significant velocity component perpendicular to the ion beam axis are still spatially discriminated against by the apertures. This ''partially discriminated'' mode closely resembles the ''steradiancy detector'' described by Baer *et al.*[44] and Spohr *et al.*[45] Under the conditions used in our study one obtains peaks with a FWHM of roughly 150 $cm^{-1}$ and an asymmetric shape, i.e., with a tail toward high electron kinetic energies. Nevertheless, this mode allows us to determine electron affinities to within $\pm 50$ $cm^{-1}$. Although sacrificing resolution the PDTP mode has the advantage of much higher electron sensitivity than the ZEKE mode.

The experiment is operated at a repetition rate of 30 Hz (20 Hz in the experiments which use the Nd:YAG laser as pump source). The ZEKE (PDTP) spectra are normalized to the ion signal and laser power, and averaged over typically 1500–4000 (200–2000) laser shots per point. Absolute vacuum wavelengths are obtained by calibration of the dye lasers, either with a New Focus 7711 Fizeau wavelength meter or a Fe/Ne hollow cathode lamp.

## III. ZEKE AND PDTP RESULTS

The ZEKE and PDTP spectra for the $Xe_nI^-$ clusters are shown in Figs. 2–5. As is clear from Fig. 1 and our earlier studies of other diatomic and polyatomic rare gas halide species, we expect to observe two sets of features separated by approximately the spin–orbit splitting $\Delta_{so}(I)$ of atomic iodine ($7603.0\,cm^{-1} = 0.942\,65$ eV).[46] The lower-energy features (Figs. 2–4) are due to transitions from the anion cluster to electronic states correlating with the $^2P_{3/2}$ ground state of the iodine atom, and those at higher energy arise from transitions from the anion cluster to states referring asymptotically to the iodine $^2P_{1/2}$ state (Fig. 5).

We first focus on the spectra for the low-energy features. Figure 2 shows the complete set of ZEKE scans taken for $n=0-12$. With an increasing number of xenon atoms the spectra appear at increasingly higher energy; i.e., they are progressively blue-shifted relative to the position of the 1.2 $cm^{-1}$ wide atomic iodine line ($n=0$). This indicates that the anion clusters are more strongly bound than the neutral species. The blue-shift decreases steadily with an increasing number of xenon atoms, indicating that the incremental stabilization of the anion decreases as the cluster grows.

All spectra for $n>0$ show a more or less pronounced double peak structure, varying between a shoulderlike ap-

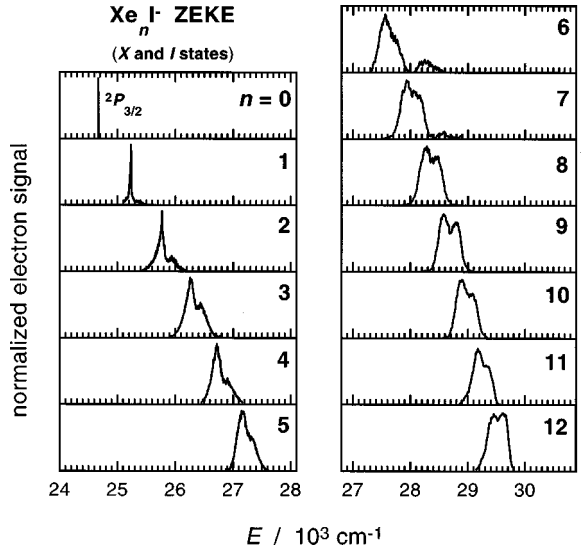


FIG. 2. The complete set of *X* and *I* state ZEKE spectra for all $Xe_nI^-$ clusters studied ($n=0-12$).

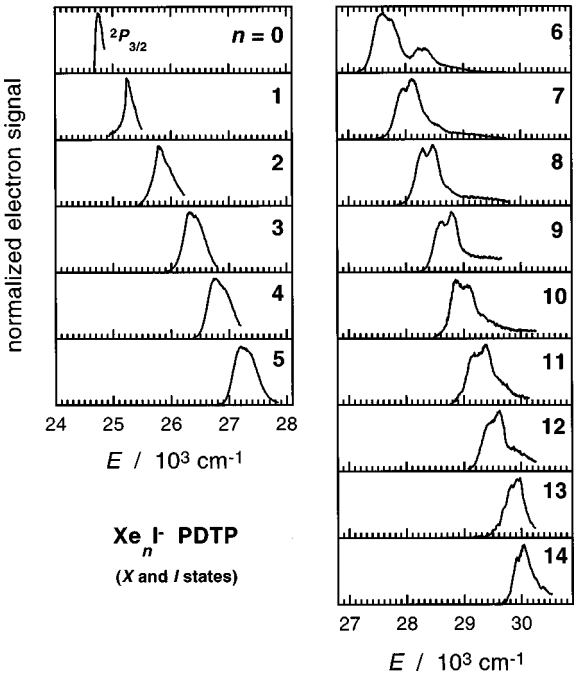


FIG. 4. The *X* and *I* state partially discriminated threshold photodetachment (PDTP) spectra for all $Xe_nI^-$ clusters studied ($n=0-14$).

pearance (e.g., $Xe_5I^-$) and a fairly clear separation of the two features (e.g., $Xe_9I^-$). Our previous work on diatomic rare gas halide species[33,37,38] and larger $Ar_nI^-$ and $Ar_nBr^-$ clusters[39] showed that these features arise from photodetachment to the *X* and *I* electronic states (see Fig. 1).

The relative intensities of the *X* and *I* state features change considerably with cluster size. For the diatomic ($n=1$) the *I* state is much weaker than the *X* state and is almost invisible in Fig. 2.[33] However, the relative intensity of the *I* state increases for $n=2$ and 3, and reaches roughly half the intensity of the *X* state for the latter cluster. Up to $n=6$ the relative intensities change only slightly, but for all clusters with $n>6$ the intensity of the *I* state feature appears to grow further, and even equals that of the *X* state for $n=12$. Also note that additional very weak features are observed at even higher energies for $n=6$ and $n=7$. The interpretation of these peaks is not yet fully understood.

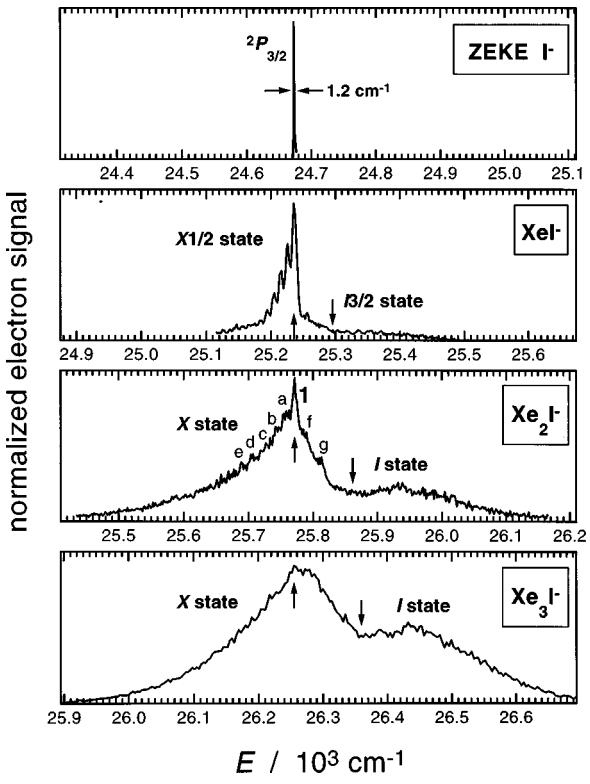


FIG. 3. The $^2P_{3/2}$ state ZEKE spectrum for iodide and $X+I$ state ZEKE spectra for $XeI^-$, $XE_2I^-$, and $Xe_3I^-$. Arrows in the $Xe_nI^-$ spectra mark positions of the 0–0 transition for the *X* and *I* state of each cluster (partly estimated). For a discussion of the marked *X* state features in the $Xe_2I^-$ spectrum see the text.

In Fig. 3 we show the ZEKE scans for the clusters $Xe_nI^-$ with $n=0-3$ in more detail. The spectrum for photodetachment to the $^2P_{3/2}$ state of iodine consists of a single peak with a FWHM of 1.2 cm$^{-1}$. To our knowledge this is the best resolution obtained so far in an anion ZEKE experiment. The $XeI^-$ spectrum was already discussed at length in our earlier study,[33] and only the most important assignments are given here. Individual peaks in this spectrum are wider than for bare iodine because of the unresolved rotational envelope. The largest peak in the spectrum, marked by an up-pointing arrow, is assigned to the 0–0 transition from the anion to the *X*1/2 state of the neutral. The peaks at lower energy, spaced by approximately 10 cm$^{-1}$, are due to sequence band transitions from higher vibrational levels of the anion. Transitions to the *I* state begin above 25 250 cm$^{-1}$; these are very weak but completely assignable.[33] In Fig. 3 the position of the *I*3/2←anion 0–0 transition is marked by a down-pointing arrow. The spacing between the two arrows directly yields an accurate $X-I$ splitting of 60.0 cm$^{-1}$ for XeI.[33] Note that this is much larger than, e.g., in the case of ArI (37.8 cm$^{-1}$).[39]

The $Xe_2I$ ZEKE spectrum is broader than the spectrum of the $XeI^-$ diatomics, however, the band envelope looks similar. As in the $XeI^-$ spectrum two main structures are observed. The first one, found below about 25 850 cm$^{-1}$, is

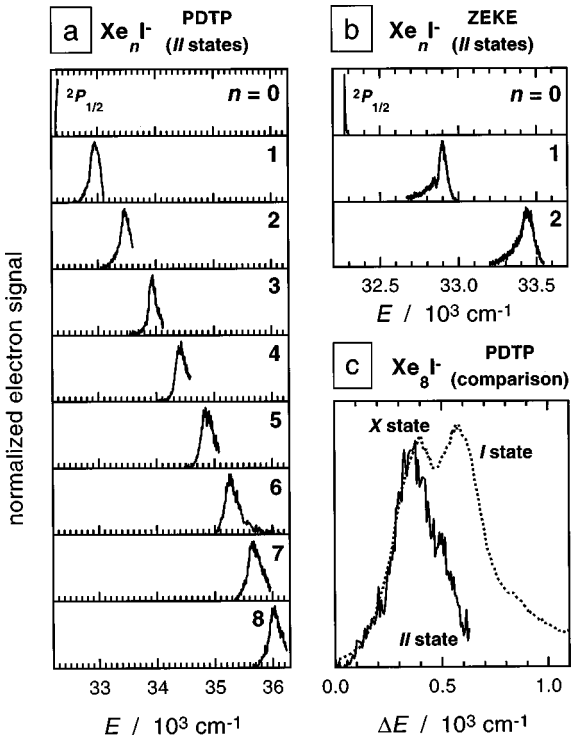


FIG. 5. ZEKE and PDTP spectra for the *II* state of the $Xe_nI^-$ clusters. (a) The PDTP spectra for $n=0-8$; (b) the ZEKE spectra for $n=0-2$; (c) a width comparison between the $Xe_8I^-$ $X+I$ state PDTP spectrum from Fig. 4 (dotted line) and the PDTP spectrum in (a) (solid line). Spectra in (c) were shifted to let the low-energy edge of both features coincide. Only the rising edge of the $I(^2P_{1/2})$ PDTP spectrum was recorded for $n=0$ in (a).

dominated by a sharp peak denoted as **1**. In analogy to $XeI^-$, we assign peak **1** to the 0–0 transition from the anion to the *X* state. This yields an accurate adiabatic electron affinity for $Xe_2I^-$ of 25 771.2 $cm^{-1}$. There are some partially resolved peaks (''a''$\cdots$''g'') visible between 25 650 and 25 850 $cm^{-1}$. Peaks ''a,'' ''b,'' and ''c'' are spaced by about 14 $cm^{-1}$ to the red of peak **1**. Peaks ''a'' and ''b'' also show a finer substructure with peak spacings of about 5 $cm^{-1}$. The spacing between the peaks ''c,'' ''d,'' and ''e'' is roughly 20 $cm^{-1}$. The location of ''a''–''e'' at energies lower than the 0–0 transition identifies these peaks as sequence band transitions. Peaks ''f'' and ''g'' are located at 25 785 and 25 810 $cm^{-1}$, respectively, and also show some substructure with a peak spacing of about 4 $cm^{-1}$.

The second (weaker and relatively unstructured) main feature, which is, however, more prominent than in $XeI^-$, is found above 25 850 $cm^{-1}$ and must be due to transitions to the *I* state. Note that the intensity of the *I* state of $Xe_2I^-$ is considerably higher than that of $XeI^-$. While a rich hot band structure in the ZEKE spectra allowed a particularly good characterization of the anion and neutral energy levels and potential curves in our earlier study of the $XeI^-$ diatomic, in the case of $Xe_2I^-$ the spectral congestion is already quite severe, which makes further assignments impossible. There is neither a clear 0–0 transition nor any other well-resolved peaks for the weaker *I* state feature. The ZEKE spectra for $n=3-12$ become even more congested, and no particularly sharp peaks can be found. The only exception is $Xe_3I^-$, also shown in Fig. 3, where some regular structure shows up in the sequence band region around 26 200 $cm^{-1}$.

This spectral congestion suggests a fairly high anion vibrational temperature, which was also observed in our study of the $XeI^-$ diatomic. The exact reason for this remains unclear. Careful optimization of the source conditions yielded only a slight reduction in vibrational temperature ($T_{vib}=130$ K compared to about 160 K in our previous study,[33] both deduced from fitting the intensities of sequence band peaks in the $XeI^-$ *X* state spectrum by assuming a Boltzmann distribution of the anion vibrational level population).

Due to the low ion signal, we were unable to obtain $X+I$ state ZEKE spectra for clusters with $n>12$. However, spectra could be taken in the PDTP mode which has the advantage of a considerably larger electron sensitivity, although at the cost of some resolution. The results for $n=0-14$ are shown in Fig. 4. While similar in appearance to the total photodetachment cross-section spectra of Becker *et al.*,[28,29] the features in our spectra are somewhat narrower. We typically obtain a FWHM of 150 $cm^{-1}$ in the PDTP mode, as can be seen in the iodine PDTP spectrum for the transition to the $^2P_{3/2}$ spin–orbit state in Fig. 4. The PDTP spectrum rises sharply at the threshold up to a maximum and then tails off toward higher energies.

With an increasing number of xenon atoms, the PDTP spectra broaden corresponding to the development of the double peak structure observed in the ZEKE spectra. Starting with $n=7$, the double peak structures also clearly appear in the PDTP spectra. Most importantly, we were able to obtain spectra for $n=13$ and 14. The blue-shift between $Xe_{12}I^-$ and $Xe_{13}I^-$ is comparable to that between $n=11$ and 12. However, the peak maximum in the PDTP spectrum for $Xe_{14}I^-$ appears at only slightly higher energies than for $Xe_{13}I^-$. While at first glance this might be associated with the closing of the first shell of xenon atoms around the iodide anion at $n=13$, the simulated annealing MD simulations presented in Sec. V will show that the situation is more complicated.

We next consider the $Xe_nI^-$ *II* state spectra shown in Fig. 5, starting with the ZEKE spectra in Fig. 5(b). The iodine $^2P_{1/2}$ spectrum ($n=0$) consists of a sharp single peak with a FWHM of about 2 $cm^{-1}$. The XeI *II* state spectrum ($n=1$) was already discussed in detail in our earlier ZEKE study.[33] The envelope of the $Xe_2I^-$ spectrum ($n=2$) looks very similar to that of the diatomic, but is relatively unstructured and therefore is not shown in greater detail. This is due to the fact that the ZEKE delay has to be reduced to get a large enough electron signal, mainly because of low laser detachment energies (frequency doubling is necessary).

No ZEKE spectra of good quality could be recorded for $n>2$. Therefore we measured additional PDTP spectra for the clusters up to $Xe_8I^-$, shown in Fig. 5(a). PDTP spectra for clusters with $n>8$ could not be obtained because at shorter wavelengths background electrons originating from the metal surfaces due to stray light became a severe problem (the work function for iron is 4.5 eV, corresponding to about 276 nm[47]).

As in Fig. 4 it is observed that the PDTP spectra are progressively blue-shifted with increasing *n*. The most striking difference is that for all clusters the width of the *II* state

TABLE I. Experimental adiabatic electron affinities, excited state origins, and electronic state splittings for $Xe_nI$. Estimated uncertainties (±) for state origins and splittings extracted from ZEKE and PDTP data are given in parentheses. All energies are in $cm^{-1}$.

| $n$ | EA[a] ($X$ state origin) | $I$ state origin[a] | $\Delta_{X-I}$ | II state origin[b] | $\Delta_{X-II}$ |
|---|---|---|---|---|---|
| 0 | 24 672.80[c] | --- | --- | 32 275.8[c,d] | 7603.0[d] |
| 1 | 25 235.9 (2.0) | 25 295.9 (3.0) | 60.0 (5) | 32 880 (5) | 7644.1 (7) |
| 2 | 25 771.2 (2.0) | 25 861 (50) | 90 (52) | 33 405 (20) | 7634 (22) |
| 3 | 26 255 (15) | 26 360 (50) | 105 (65) | 33 879 (20) | 7624 (35) |
| 4 | 26 711 (20) | 26 818 (50) | 107 (70) | 34 336 (30) | 7625 (50) |
| 5 | 27 149 (20) | 27 259 (50) | 110 (70) | 34 774 (30) | 7625 (50) |
| 6 | 27 556 (30) | 27 683 (50) | 127 (80) | 35 181 (40) | 7625 (70) |
| 7 | 27 931 (30) | 28 065 (50) | 134 (80) | 35 566 (40) | 7635 (70) |
| 8 | 28 262 (40) | 28 394 (50) | 132 (90) | 35 936 (40) | 7674 (80) |
| 9 | 28 572 (50) | 28 707 (50) | 135 (100) | --- | --- |
| 10 | 28 880 (50) | 29 006 (50) | 126 (100) | --- | --- |
| 11 | 29 175 (50) | 29 289 (50) | 114 (100) | --- | --- |
| 12 | 29 443 (50) | 29 558 (50) | 115 (100) | --- | --- |
| 13 | 29 780 (70) | --- | --- | --- | --- |
| 14 | 29 900 (70) | --- | --- | --- | --- |

[a] $n=1-12$ extracted from the ZEKE spectra; $n=13$ and 14 from the PDTP spectra; see the text.
[b] $n=1$ from the ZEKE spectrum; $n=2-8$ from the PDTP spectra; see the text.
[c] Reference 49.
[d] Reference 46.

PDTP spectra is considerably smaller, because only a single electronic state contributes to the signal. For the $Xe_8I^-$ cluster this is demonstrated in Fig. 5(c), which compares the PDTP spectrum for the $Xe_8I^-$ $X$ and $I$ states from Fig. 4 (dotted line) and the $II$ state spectrum from Fig. 5(a) (solid line).

The question arises of how to extract reliable values for the adiabatic detachment energies (ADEs) for the $X$ and $I$ state from the cluster spectra. For the ZEKE spectra in Figs. 2 and 3 this was done by fitting the observed spectral features to the sum of two Gaussian functions with variable position, amplitude, and width by employing a Levenberg–Marquardt least squares fitting procedure.[48] In the $XeI^-$ and $Xe_2I^-$ spectra, the maximum of the $X$ band corresponds approximately to the ADE. We therefore assume that the position of the maximum for the lower-energy Gaussian peak gives a sufficiently precise estimate for the ADE of the $X$ state (in other words, the adiabatic electron affinity of each cluster). The reliability of this procedure was checked by convoluting the $X$ state ZEKE spectra of $XeI^-$ and $Xe_2I^-$ (Figs. 2 and 3) with a Gaussian of 10–20 meV FWHM to mimic the progressively broader features appearing in the ZEKE spectra of the larger clusters. It was found that the maximum position of the Gaussian convolution and the accurately known $X$ state 0–0 transitions in the ZEKE spectra of $XeI^-$ and $Xe_2I^-$ (Table I) agree very well.

For $n=13$ and 14 only the PDTP spectra are available (Fig. 4). For $n=12$, the PDTP spectrum exhibits a shoulder at the same position where the $X$ state peak of the corresponding ZEKE spectrum is located (Fig. 2). We therefore estimated the ADEs for $n=13$ and 14 from the position of the shoulder to the left of the maximum in each PDTP spectrum (see Table I).

The location of the 0–0 transition in the ZEKE spectra of the $I$ states is less obvious: our earlier spectral simulations of the $I$ state ZEKE spectrum of $XeI^-$[33] located it on the low-energy side of the electronic band. Here we convoluted the best fit vibrational stick spectrum from our earlier study with a Gaussian of 8 meV, which resulted in a $I$ state spectrum of approximately Gaussian shape and similar in appearance to those of the clusters $Xe_2I^-$ and $Xe_3I^-$ in Figs. 2 and 3. It was found that the very accurately known XeI $X-I$ splitting obtained from the $XeI^-$ ZEKE spectrum corresponds to about 60% of the value obtained when taking the energetic spacing between the $X$ state 0–0 transition and the maximum of the simulated $I$ state band. Assuming the same behavior for the spectra of the larger clusters in Figs. 2 and 3, we consistently estimated the $X-I$ splitting as 60% of the spacing of the fitted Gaussian peaks. The resulting experimental electron affinities, $I$ state 0–0 transitions (ADEs) and $X-I$ splittings obtained from this procedure are summarized in Table I, together with estimated error bars.

The $II$ state 0–0 transitions were extracted from the PDTP spectra in Fig. 5 by taking the $XeI^-$ $II$ state ZEKE spectrum with its known 0–0 transition[33] as a reference. The $XeI^-$ PDTP spectrum was superimposed, and it was found that for this particular cluster the 0–0 transition in the ZEKE spectrum is located at the energy, where the PDTP spectrum reaches 62% of its maximum. For all the other $II$ state PDTP spectra this value was taken as the reference point. The extracted energies for the $II$ state 0–0 transitions are also given in Table I together with the $X-II$ splittings and estimated uncertainties. The EAs, state origins, and splittings will be discussed in greater detail together with results from the simulated annealing MD calculations in Sec. V.

## IV. SIMULATION OF EXPERIMENTAL RESULTS

In this section we discuss our methodology for setting up model potentials for the anion and neutral clusters and then

TABLE II. MMSV pair potential parameters for XeI and $XeI^-$. ''Set I''=the original set from Ref. 33; ''Set II''=but shifted by +0.25 Å and refitted to the MMSV-type model potential. Note that both potential sets yield identical spectral fits for the $X1/2$, $I3/2$, and $II1/2$ state ZEKE spectra of $XeI^-$ (Ref. 33).

| | Set I | | | | Set II | | | |
|---|---|---|---|---|---|---|---|---|
| | $X1/2$ | $I3/2$ | $II1/2$ | Anion | $X1/2$ | $I3/2$ | $II1/2$ | Anion |
| $\epsilon$ (meV) | 33.07 | 25.06 | 27.48 | 103.2 | 33.07 | 25.06 | 27.48 | 103.2 |
| $R_m$ (Å) | 4.049 | 4.34 | 4.24 | 4.09 | 4.30 | 4.59 | 4.49 | 4.34 |
| $\beta_1$ | $16.8896-8.455\,66\cdot R+1.420\,29\cdot R^2$ | 7.20 | 5.20 (6.88)[a] | 3.79 | $17.8625-8.487\,40\cdot R+1.347\,30\cdot R^2$ | 7.62 | 5.51 (7.41)[a] | 4.02 |
| $\beta_2$ | 6.29 | 5.95 | 7.10 | 6.03 | 6.60 | 6.23 | 7.37 | 5.56 |
| $x_1$ | 1.091 | 1.100 | 1.095 | 1.010 | 1.424 | 1.182 | 1.010 | 1.189 |
| $x_2$ | 1.753 | 1.588 | 1.635 | 1.430 | 1.998 | 1.998 | 2.000 | 1.686 |
| $C_6$ (eV Å$^6$) | 185.5 | 198.4 | 192.0 | --- | 185.5 | 198.4 | 192.0 | --- |
| $C_8$ (eV Å$^8$) | 1982 | 2148 | 2065 | --- | 1982 | 2148 | 2065 | --- |
| $B_4$ (eV Å$^4$) | --- | --- | --- | 28.98 | --- | --- | --- | 28.98 |
| $B_6$ (eV Å$^6$) | --- | --- | --- | 365.4 | --- | --- | --- | 365.4 |

[a]The value in parentheses used in the simulated annealing MD calculations; see the text.

finding the minimum energy structures based on these potentials. From these we can determine theoretical electron affinities and electronic state splittings that can be compared directly to experiment. Figure 1 illustrates the connection between theoretical and experimental quantities. The electron affinity $EA(Xe_nI)$ of a $Xe_nI$ cluster is given by

$$EA(Xe_nI)=EA(I)+\epsilon_{an}-\omega_0^{an}-\epsilon_X+\omega_0^X, \tag{3}$$

where EA(I) is the electron affinity of atomic iodine ($24\,672.796\,cm^{-1}=3.059\,038\,eV$),[49] $\epsilon_{an}$ and $\epsilon_X$ are the classical binding energies (well depths), and $\omega_0^{an}$ and $\omega_0^X$ are the zero-point energies of the anion and $X$ state, respectively. The experimental $X-I$ splitting, defined with respect to the vibrational ground states, can be obtained via

$$\Delta_{X-I}=\epsilon_X-\omega_0^X-\epsilon_I+\omega_0^I, \tag{4}$$

and the $X-II$ splitting in an analogous manner by

$$\Delta_{X-II}=\epsilon_X-\omega_0^X-\epsilon_{II}+\omega_0^{II}+\Delta_{so}(I). \tag{5}$$

Here $\Delta_{so}(I)$ is the spin–orbit splitting of atomic iodine ($0.94265\,eV=7603.0\,cm^{-1}$).[46] To evaluate Eqs. (3)–(5) sufficiently, accurate model potential functions are needed. Using these, the minimum energy cluster geometries as well as zero-point energies have to be determined.

### A. Two-body potential functions

Just as in our previous fitting[33] of the ZEKE spectra of diatomic $XeI^-$, we used a flexible, piecewise Morse–Morse-switching function–van der Waals (MMSV) potential. For neutral XeI, the reduced form of this potential [with $f(x)=V(R)/\epsilon$ and $x=R/R_m$] is

$$\begin{aligned} f(x)&=e^{2\beta_1(1-x)}-2e^{\beta_1(1-x)}, \quad 0<x\leqslant 1,\\ &=e^{2\beta_2(1-x)}-2e^{\beta_2(1-x)}\equiv M_2(x), \quad 1<x\leqslant x_1,\\ &=SW(x)M_2(x)+[1-SW(x)]W(x), \quad x_1<x<x_2,\\ &=-C_{6r}x^{-6}-C_{8r}x^{-8}\equiv W(x). \quad x_2\leqslant x<\infty. \end{aligned} \tag{6}$$

The switching function $SW(x)$ is given by

$$SW(x)=\frac{1}{2}\left(\cos\frac{\pi(x-x_1)}{(x_2-x_1)}+1\right), \tag{7}$$

and the reduced dispersion coefficients $C_{nr}$ take the form

$$C_{6r}=\frac{C_6}{\epsilon R_m^6}, \quad C_{8r}=\frac{C_8}{\epsilon R_m^8} \tag{8}$$

where $R_m$ represents the equilibrium bond length (position of the well minimum) and $\epsilon$ is the potential well depth. $C_6$ is the induced dipole–induced dipole dispersion coefficient, and $C_8$ represents the corresponding coefficient for the induced dipole–induced quadrupole interaction.

For the $XeI^-$ anion potential the same functional form was used, except that the dispersion terms were replaced by

$$f(x)=-B_{4r}x^{-4}-B_{6r}x^{-6}\equiv W(x), \quad x_2\leqslant x<\infty, \tag{9}$$

with

$$B_{4r}=\frac{B_4}{\epsilon R_m^4}, \quad B_{6r}=\frac{B_6}{\epsilon R_m^6} \tag{10}$$

and

$$B_4=\tfrac{1}{2}q^2\alpha_d(Xe), \quad B_6=\tfrac{1}{2}q^2\alpha_q(Xe)+C_6. \tag{11}$$

$q$ is the iodide charge and $B_4$ represents the coefficient of the leading term in the long range $XeI^-$ potential, reflecting the dipole induced in the xenon atom by the iodide anion. The two contribution to $B_6$ are from quadrupole induction and dipole dispersion. $\alpha_d(Xe)$ and $\alpha_q(Xe)$ are the dipole and quadrupole polarizabilities of the xenon atom, respectively. Further details about the construction of the $XeI^{(-)}$ two-body potentials can be found in our earlier publication.[33]

The original potential parameters for the XeI diatomic potentials are included in Table II, denoted as ''Set I.'' As discussed previously,[33] the diatomic ZEKE spectra are sensitive only to *changes* in the well depth $\epsilon$ and equilibrium internuclear separation $R_m$ upon photodetachment. During the current work an improved set of potential parameters, denoted as ''Set II'' (also included in Table II), was found that better describes the size-dependent electron affinities for the largest clusters, as will be discussed further in Sec. V.

The new set was obtained by simply increasing $R_m$ for *all* potentials of ''Set I'' by 0.25 Å and refitting these shifted curves to the MMSV potential form of Eq. (6). This means that the well depth and the shape in the Franck–Condon region, as well as the relative position of all the potentials, remained unchanged. Both sets of potentials therefore yield indistinguishable Franck–Condon simulations for the $X1/2$, $I3/2$, and $II1/2$ state ZEKE spectra of $XeI^-$. Thus, all the spectral assignments and conclusions drawn in our earlier publication[33] remain valid for our new set of potentials.

While the absolute position of each potential in the original ''Set I'' was based on the $X1/2$ state potential for XeI from emission studies by Tellinghuisen and co-workers ($R_m = 4.049$ Å),[50] the new set can be seen as referenced to the position of Lee's $X1/2$ state scattering potential ($R_m = 4.30$ Å),[51] while still keeping the improved well depth and shape of the Tellinghuisen potential. Note also that for ''Set II'' the $R_m$ value of the $I$ state potential ($R_m = 4.59$ Å) is now almost identical to Lee's value ($R_m = 4.60$ Å) and the equilibrium bond length and well depth of the $XeI^-$ anion potential ($R_m = 4.34$ Å, $\epsilon = 103.2$ meV) is in perfect agreement with the very recent CCSD(T) calculations by Schröder *et al.* ($R_m = 4.34$ Å, $\epsilon = 100$ meV).[52]

In addition to the XeI and $XeI^-$ pair potentials, a Xe–Xe potential is required. For this we used the accurate Hartree–Fock dispersion (HFD-B2) potential of Aziz, Meath, and coworkers ($R_m = 4.3656$ Å and $\epsilon = 24.37$ meV).[53]

The pairwise additive approximation to the $Xe_nI^-$ binding energies was found by minimizing the additive potentials using the simulated annealing MD simulations described below via

$$\epsilon_{an} = \min(V_{Xe-I^-} + V_{Xe-Xe}), \tag{12}$$

where

$$V_{Xe-I^-} = \sum_i V_{i0}(|\mathbf{r}_i - \mathbf{r}_0|) \tag{13}$$

and

$$V_{Xe-Xe} = \sum_{i<j} V_{ij}(|\mathbf{r}_i - \mathbf{r}_j|). \tag{14}$$

The sums run over the xenon atoms; $\mathbf{r}_i$ is the position of the xenon atom $i$, and $\mathbf{r}_0$ is the position of the iodide anion.

The calculation of the $Xe_nI$ neutral potentials is more complex due to the open-shell nature of the iodine atom. As in studies of other groups[4,54–59] and our earlier work on polyatomic rare gas–halogen clusters,[39] we used a first-order perturbation theory treatment of the interaction of the open-shell iodine atom with several xenon atoms in terms of the diatomic XeI potentials. The resulting potentials are frequently referred to as ''matrix additive'' (due to the $6\times6$ matrix structure of the perturbation Hamiltonian[4,58,59]), and this term will be used below.

The model itself was deduced under the assumption of $R$-independent spin–orbit splitting for the halogen atom. In the current study it was found necessary to adjust the repulsive wall of one of the neutral diatomic potentials to fulfill this requirement because at very short range the original XeI $X$, $I$, and $II$ state potentials yield an iodine spin–orbit coupling constant $\Delta_{so}(I)$ slightly smaller than in atomic iodine.[60–62] This was achieved by slightly increasing the $\beta_1$ parameter for the $II$ state potentials in both potential parameter sets. The values obtained this way are given in parentheses in Table II.

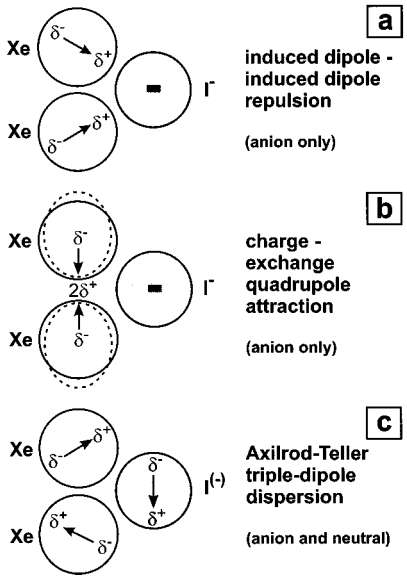


FIG. 6. A pictorial representation of selected many-body effects for $Xe_2I^{(-)}$. (a) Induction nonadditivity (repulsion between induced dipoles); (b) the attraction between the iodide charge and the exchange quadrupole of two xenon atoms; (c) Axilrod–Teller triple-dipole dispersion: this is repulsive for the triangular arrangement shown here, but attractive for the linear configuration. The most important effect is the destabilization of the anion cluster by induction nonadditivity.

## B. Many-body interactions

In the following we only briefly summarize those many-body interactions most important in the systems studied here. Simplified schematics of the most important effects are given in Fig. 6 and will be discussed below. Further details can be found in the Appendix and in our earlier publication.[39]

From Eq. (3) we expect that the experimentally measured electron affinity of the cluster will be most sensitive to nonadditive effects occurring only in the anion *or* neutral cluster. In contrast, effects occurring both in the anion and neutral act in the same direction, i.e., either both stabilize or both destabilize the respective cluster, which results in a much smaller net effect on the electron affinity.

### *1. Nonadditive induction in the anion*

Based on our earlier results for the $Ar_nI^-$ and $Ar_nBr^-$ systems,[39] we expect the largest nonadditive effect in $Xe_nI^-$ to arise from the interaction between multipole moments induced in the xenon atoms by the iodide charge. Figure 6(a) shows a ''cartoon'' of this effect for $Xe_2I^-$ in a triangular arrangement. The iodide anion induces dipole moments in both xenon atoms, and the induced dipoles repel one another, yielding a net reduction of the binding energy. The anion is therefore destabilized and the electron affinity decreases.

We include nonadditive charge-induced dipole and charge-induced quadrupole contributions in the framework

of the ''full iteratively calculated induction model'' (see the Appendix for more details and specific parameters). As in our earlier work, due to the high computational expense for the substantial number of MD runs required, a simpler model was used in which the interaction energy between dipoles directly induced in the xenon atoms by the iodide charge is calculated.[39,63] The minimum energy structures found with the simple model were optimized using the full iteratively calculated induction model.

#### 2. Charge-exchange quadrupole interactions in the anion

The charge–exchange quadrupole interaction, sketched in Fig. 6(b) for the case of $Xe_2I^-$, is due to the interaction of the iodide charge with the $Xe_2$ exchange quadrupole. This quadrupole results from the redistribution of electron density in the region between the two xenon nuclei in order to reduce overlap repulsion.[64] Compared to the electron density in the absence of exchange repulsion, the net effect can be approximated as a positive partial charge $+2\delta$ between the xenon atoms and two negative partial charges $-\delta$ at each xenon nucleus. The first nonvanishing moment for two identical atoms is a quadrupole. Because the positive partial charge is closer to the iodide anion, the net effect is an attractive force, resulting in an increase of the cluster binding energy, i.e., a stabilization of the anion cluster relative to the situation where only two-body forces are acting. To model this effect we use the ''Gaussian exchange charge'' formalism (see the Appendix).

#### 3. Charge-dispersion multipole interactions in the anion

There are also multipole moments induced in the xenon atoms due to dispersion that interact with the iodide charge. As in our earlier work we calculated the dipole and quadrupole moments induced in the xenon atoms using the model of Hunt[65] in terms of atomic polarizabilities and dispersion coefficients; more details can be found in the Appendix.

#### 4. Axilrod–Teller triple-dipole interaction (anion and neutral)

The Axilrod–Teller triple-dipole interaction (DDD)[66–68] is a pure dispersion effect and therefore present both in the anion and the neutral. The effect arises from the change in mutual polarization of two atoms by the presence of a third atom and is attractive for a linear $Xe–I^{(-)}–Xe$, though repulsive for a triangular $Xe_2I^{(-)}$ arrangement [shown in Fig. 6(c)]. Note that the latter type of arrangement is the dominant structural element in both the anion and neutral $Xe_nI^{(-)}$ clusters. For specific details see the Appendix.

We do not include triple-dipole terms for Xe–Xe–Xe, because they are expected to be almost identical in the anion and neutral clusters. We also neglect higher multipole three-body dispersion terms such as the dipole–dipole–quadrupole potential (DDQ). For $Ar_nI$ and $Ar_nBr$ the DDQ effect was estimated to be $<50\%$ of the size of the DDD contribution. Moreover, the net effect for the electron affinities for all nonadditive dispersion terms is expected to be even smaller. This is due to the fact that the electron affinity is only sensitive to the *difference* in the anion and neutral DDD (DDQ, ...) contributions [see Eq. (3)]. Finally, we neglect three-body exchange effects, which are also present in both the anion and the neutral, because they are expected to be small.[39]

### C. Simulated annealing MD calculations

Our particular implementation to locate global and local minimum energy anion cluster geometries uses a flexible simulated annealing MD algorithm,[39] which can be briefly summarized by the following steps.

(1) *Selection of initial conditions:* Random initial xenon and iodide positions are selected within a 6–18 Å box, depending on the cluster size. As a constraint no two atoms may be closer than 3.5 Å to prevent the evaporation of atoms starting in a highly repulsive region of the potential energy surface.

(2) *Quenching:* Kinetic energy is removed very quickly by rescaling the atomic velocities, i.e., the cluster is rapidly quenched into a nearby minimum on the potential energy surface.

(3) *Simulated annealing:* Starting with the minimum energy configuration of step (2), a randomly selected portion of kinetic energy (restricted usually to 5%–35% of the classical binding energy) is added. The system is then cooled by gradually removing kinetic energy until the lowest energy state is reached. Variable ''annealing schedules'' with a length of up to 10 ns and a (within reasonable bounds) randomly selected annealing velocity are used. (Note that theoretically simulated annealing will *always* find the global minimum if the cooling schedule is slow and the trajectory infinitely long.)[69]

(4) *Gradient minimization* is used to locate the minimum energy structure obtained from step (3) more precisely.

(5) Steps (1)–(4) are repeated up to 1000 times, depending on the cluster size and potential model applied.

In contrast to our earlier study,[39] the complete algorithm [steps (1)–(5) and the cluster normal mode analysis mentioned below] is now contained in a single program package. Moreover, the number of trajectories [step (5)] was increased by more than a factor of 50, which allows us to obtain a complete survey of all the relevant global and local cluster minima. Most of the quantities, especially those controlling the annealing run [step (3)], are now chosen randomly to search the cluster potential energy surface in an unbiased way.

Interestingly, for the anion clusters with $n \leqslant 12$, it was found in this study that rapidly quenching a large enough number of random starting configurations alone [i.e., without the annealing step (3)] was equally well suited to find the global minimum and the most important local minima on the potential energy surface. The interaction between xenon and the iodide anion is more than four times stronger than that between two xenon atoms, and therefore $Xe_nI^-$ structures which maximize the number of $Xe–I^-$ bonds are energetically favored. This seems also to affect the topology of the cluster hypersurface in a way that these structures are easily reached within a moderate number of simple quenching steps.

Because we are interested in adiabatic electron affinities and detachment energies, the neutral *X*, *I*, and *II* state configurations are obtained by relaxing the optimized anion geometry on the respective neutral potential energy surface. Finally, zero-point energies for the anion and neutral clusters are determined using the ''anharmonic normal mode analysis,'' as described in our earlier paper.[39] Electron affinities and the other detachment energies can then be calculated via Eq. (3) and the analogous expressions for the *I* and *II* states.

## V. ANALYSIS AND DISCUSSION

### A. Electron affinities

In the following section we discuss our experimental findings for the cluster-dependent electron affinities (EAs) and compare these results with electron affinities calculated from the model potentials. This is done first for the anion pair potentials and the matrix additive *X* state potentials, for which anion and neutral minimum energy structures are found using the MD simulation procedure described above. After that, the different many-body effects are added successively, and the MD procedure is repeated to find the lowest-energy structures for the resulting model potentials. Note that all calculations in this section use the two-body potential parameter ''Set II'' given in Table II. A complete compilation of cluster energies and individual potential term contributions is available from the authors upon request.

First, we focus on the experimental electron affinities as a function of cluster size, depicted in Fig. 7(a) (''□''). With increasing *n*, the electron affinities increase due to the increasing stabilization of the anion relative to the *X* state. The EA curve shows a pronounced decrease in slope toward large *n*, with a particularly significant decrease in slope at $n=13$ (see also Table I). This will be discussed in more detail in Sec. V C.

Next, we consider the simulations based on a simple pair potential for the anion and the matrix additive potential for the *X* state, completely neglecting many-body effects. These results are shown in Fig. 7(a) and also in Fig. 7(b) in terms of *differences* between the calculated and experimental values (''▲''). As *n* increases, the calculated EAs become significantly larger than the experimental values. Note also that for the pair potential the drop in the EA slope occurs at $n=12$ rather than $n=13$.

In the next step the nonadditive induction effect is added to the anion model potential (the *X* state model potential does not change). These results are shown in Fig. 7(b) (''○''), but are not included in Fig. 7(a) for the sake of clarity. Most importantly, a significant decrease in the EAs is observed, which is mainly due to repulsion of adjacent induced dipoles on the xenon atoms. There is also a repulsion between adjacent induced quadrupoles; however, this effect contributes only about 9% of the total induction effect. Including the nonadditive induction improves the agreement with the experimental EAs, but overcorrects the results obtained for the pair potentials, resulting in a deviation of opposite sign (e.g., about $-400$ cm$^{-1}$ for $n=14$).

Inclusion of nonadditive induction and both the charge-exchange quadrupole and charge-dispersion multipole interactions leads to the results shown in Fig. 7(b) (''▽''). The net increase of the calculated EAs is due to the dominant charge-exchange quadrupole contribution, which stabilizes the anion. In contrast, the charge-dispersion dipole interaction is opposite in sign and roughly a factor of 2 smaller. The charge-dispersion quadrupole term is small and could be neglected without any significant loss of accuracy. Inclusion of these three nonadditive effects yields slightly larger EAs than found in the experiments (e.g., roughly $+200$ cm$^{-1}$ for $n=12$).

Finally, we add in the Axilrod–Teller triple-dipole dispersion. This leads to the size-dependent EAs shown in both Figs. 7(a) and 7(b) (''●''). The Axilrod–Teller term is more repulsive for the anion than for the neutral due to the larger polarizability of the iodide anion relative to neutral iodine, which results in a larger $C_9$ coefficient. Consequently, a greater destabilization of the anion relative to the *X* state is observed, which leads to a decrease of the calculated EAs for all clusters, bringing them very close to the experimental values. [Note that the experimental uncertainties from Table I have been included in Fig. 7(b) as shaded regions.]

The contributions of the various effects to the total classical binding energy at the equilibrium structure of each cluster are shown in Fig. 8(a) for the $Xe_nI^-$ anions and in Fig. 8(b) for the $Xe_nI$ *X* states. The observed trends are largely

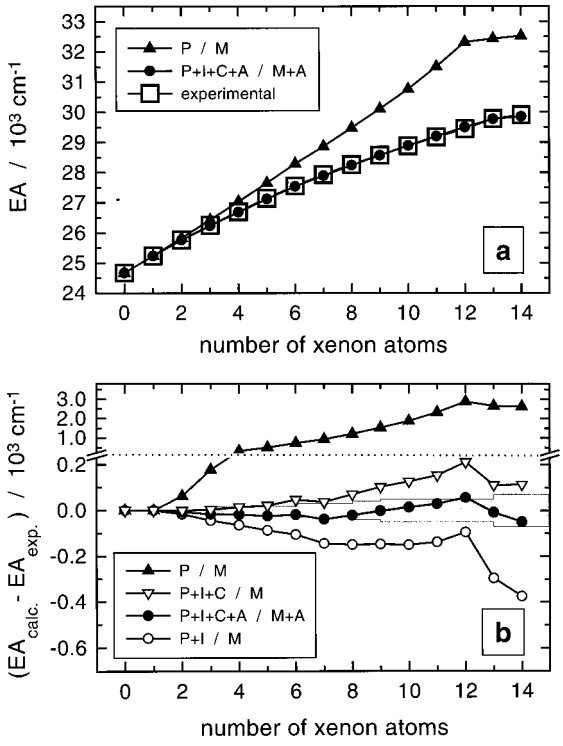


FIG. 7. (a) A comparison of size-dependent experimental electron affinities with those calculated from different potential models. ''□:'' experimental data from Table I; ''▲:'' pair potential (abbreviation ''P'') for an anion, matrix additive potential (M) for the *X* state; ''●'': P+nonadditive induction (I)+exchange/dispersion multipole-charge interactions (C)+Axilrod–Teller (A) for an anion, M+A for the *X* state; (b) differences between calculated and experimental electron affinities: ''▲'' and ''●'' as in (a); ''▽'': P+I+C for an anion, M for the *X* state; ''○:'' P+I for an anion, M for the *X* state. Uncertainties of the experimental EAs from Table I are shown as grey-shaded regions.

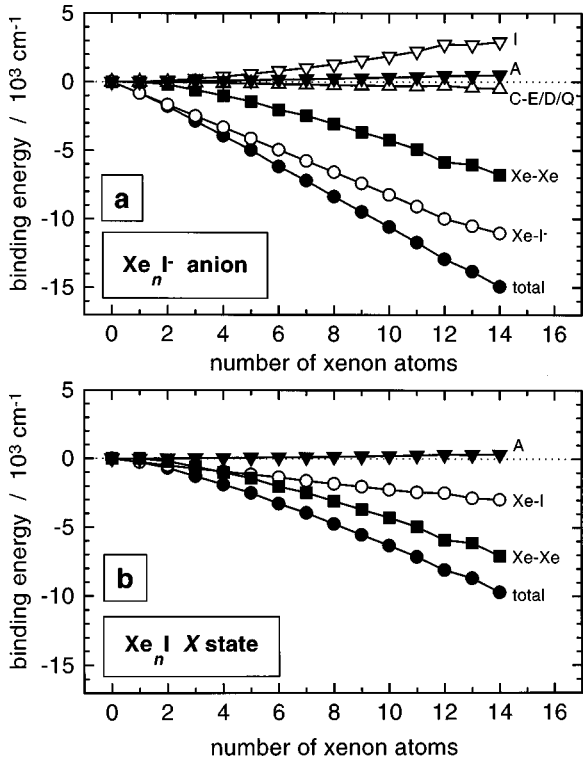


FIG. 8. Contributions to the total classical binding energies for the $Xe_nI^-$ anion clusters (a) and the $Xe_nI$ *X* state clusters (b) extracted from the simulated annealing MD calculations, including all nonadditive potential terms. ''●:'' total classical binding energy; ''○:'' the $XeI^{-1}$ (XeI) contribution for an anion (neutral); ''■:'' a Xe–Xe contribution; ''△:'' *combined* charge–exchange quadrupole, charge–dispersion dipole and charge–dispersion quadrupole contributions (''C-E/D/Q''); ''▼:'' Axilrod–Teller triple-dipole dispersion; ''▽:'' nonadditive induction.

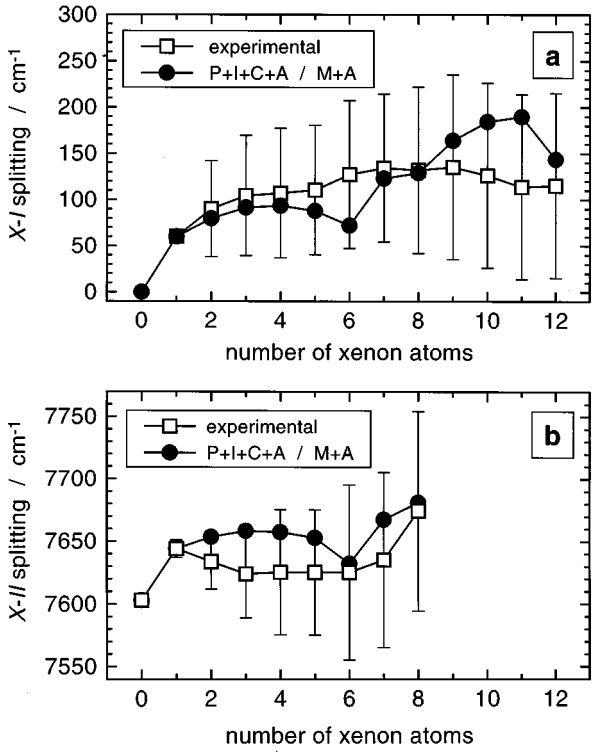


FIG. 9. Experimental and calculated neutral state splittings. (a) $X-I$ splitting; (b) $X-II$ splitting. ''□:'' experiment (Table I); ''●:'' simulation including all many-body effects (abbreviations for potential models as in Fig. 7). Uncertainties of the experimental splittings from Table I are included as error bars.

consistent with our earlier results for $Ar_nI^{(-)}$ and $Ar_nBr^{(-)}$, where many-body induction in the anion cluster was also found to be the largest nonadditive effect.[39] However, due to the much higher polarizability of xenon relative to argon the effect is much more pronounced for xenon clusters, and, in general, the neglect of many-body interactions leads to a larger deviation from the experimental results in the xenon-based clusters. For example, with pair potentials only, the calculated EA for $Ar_{12}I$ differs from the experimental EA by $+560$ cm$^{-1}$,[39] compared to a deviation of $+2880$ cm$^{-1}$ for $Xe_{12}I$. The latter deviation is clearly larger, even when scaled by the change of the electron affinities $[EA(n=12) - EA(n=0)]$, which is 2230 cm$^{-1}$ for argon and 4770 cm$^{-1}$ for xenon.

### B. Neutral *X–I* and *X–II* state splittings

In Fig. 9 we compare the splittings for the different neutral states obtained from experiment (Table I) and the potential models with all many-body options included. The $X-I$ state splittings are shown in Fig. 9(a). The general agreement between experiment and simulation is very good, especially if one keeps in mind that the experimental values extracted by the procedure described in Sec. III are only approximate (see error bars). Overall, the simulated annealing MD calculations support the assignment of the *X* and *I* states to the broad double peak features observed in the experimental ZEKE and PDTP spectra (Figs. 2–4). This assignment is further supported by the presence of only a single peak in the PDTP spectra, where transitions to the *II* states are seen (see Fig. 5 and the discussion in Sec. V D).

In Fig. 9(b) the results for the $X-II$ splittings are shown. Again good agreement between experiment and simulation is found when taking the error bars into account. However, all experimental values for $n>1$ appear to be lower than those obtained from the simulations. This is not unexpected and might be due to a decrease of the iodine spin–orbit coupling constant $\Delta_{so}(I)$ in the cluster, which has been observed in iodine-doped xenon matrices and crystals[4] as well as in our ZEKE study of the XeI diatomic.[33] In contrast, for our simulations the same spin–orbit coupling constant as for atomic iodine was assumed.

### C. Improved absolute Xe–I$^{(-)}$ bond lengths from $Xe_nI^-$ ZEKE and PDTP spectra

The energetics as a function of cluster size provide an absolute—albeit indirect—measure of the equilibrium bond distances in $XeI^-$ and XeI. A larger $XeI^{(-)}$ equilibrium bond length favors a higher coordination number of xenon atoms in the first shell around the central iodine atom than a shorter bond length. This uniquely affects the structure and energetics of both the anion and neutral $Xe_nI^{(-)}$ clusters and is expected to have a pronounced influence on the size-dependent EAs.

We therefore systematically studied the slope of the $EA(n)$ curve as a function of the $XeI^{(-)}$ bond lengths. Simu-

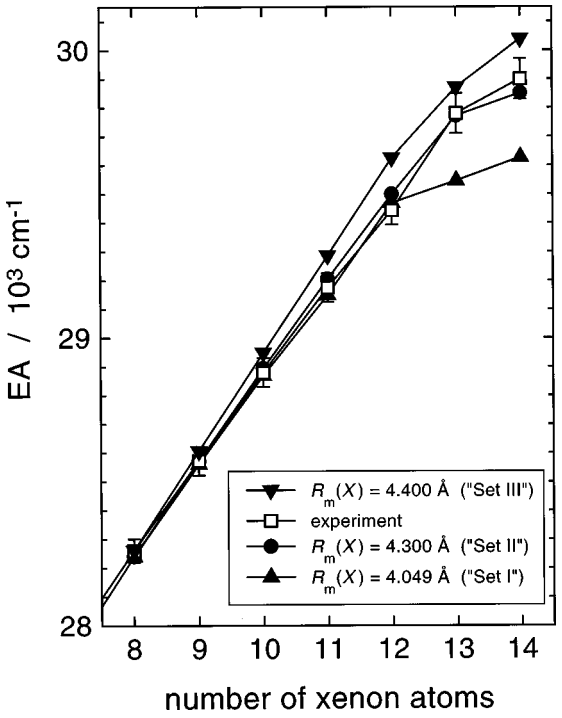


FIG. 10. A comparison of experimental and calculated electron affinities based on different sets of $Xe–I^{(-)}$ two-body potential parameters. ''□:'' experimental; ''●:'' calculated using the $XeI^{(-)}$ two-body potentials of ''Set II'' in Table II, including *all* many-body-options; ''▲:'' the same, but using ''Set I'' from Table II; ''▼:'' the same, but using ''Set III'' with $R_m(X) = 4.40$ Å; in the latter two cases, the Gaussian range parameter $\beta$ (see the Appendix) was slightly changed to 0.72 and 0.79 $Å^{-1}$, respectively.

lated annealing MD calculations for the $Xe_nI^{(-)}$ clusters were carried out for a variety of potential parameter sets. The anion, *X, I,* and *II* potential curves for different sets had exactly the same *relative* position and shape in the Franck–Condon region. However, all potentials belonging to a specific set were shifted by the same amount on the *R* axis. Here we deal with three specific examples: those denoted as ''Set I'' and ''Set II'' in Table II [$R_m(X) = 4.049$ Å and 4.30 Å, respectively], as well as ''Set III'' (not included in Table II) with even larger equilibrium bond lengths [$R_m(X) = 4.40$ Å]. ''Set II'' is the one that was used to obtain all the results discussed in the earlier sections. ''Set I'' represents the original anion, *X, I,* and *II* state two-body MMSV potential functions, as used in our earlier ZEKE study of the $XeI^-$ diatomic.[33] ''Set III'' is one of six additional sets with a $R_m$ for the *X* state between 4.05 and 4.44 Å, which we tested in the course of this study. In all cases the *X, I,* and *II* state ZEKE spectra of the $XeI^-$ diatomic are fit equally well by these different potential parameter sets.

A comparison of the EA curves for $n \geqslant 8$ obtained using Sets I–III is shown in Fig. 10. The experimental EAs and their error bars from Table I are also included. Note that for each simulation all many-body terms in the potential are utilized. For $n \leqslant 9$, the three sets of potential parameters yield almost the same (good) agreement with experiment. However, a pronounced difference is observed for $n = 13$ and 14, where ''Set II'' still gives an optimal description, while the EAs of ''Set I'' substantially underestimate the experimental values and clearly lie outside the error bars. The same deviation persists for all sets with approximately $R_m(X) \leqslant 4.25$ Å. In contrast, all potentials sets with $R_m(X) > 4.36$ Å systematically overestimate the experimental EAs for larger cluster sizes, as can be seen for $n = 11–14$ with ''Set III'' in Fig. 10.

Our systematic study therefore allowed us to determine the *absolute* position of the $Xe–I^{(-)}$ *diatomic* potential functions with much higher precision: The potential curves in ''Set II'' should have an estimated uncertainty of $\Delta R_m = \pm 0.05$ Å, which corresponds to a roughly six-fold improvement compared to the uncertainties in the absolute positions extracted on basis of the $XeI^-$ diatomic ZEKE spectra alone.[33]

The sharp change in slope for ''Set I'' in Fig. 10 is largely due to the specific structures of the anion clusters for $n \geqslant 12$, which are all based on an icosahedral motif with 12 xenon atoms forming the first shell around the central iodide anion. The additional one (two) xenon atom(s) for $n = 13$ (14) are placed on the outside of the first shell, and are more loosely bound because they are much farther away from the iodide anion. This reduces the additional stabilization of the anion clusters considerably when adding a 13th and 14th xenon atom and therefore produces the abrupt change of slope for the size-dependent EAs. In contrast, structures with more than 12 atoms in the first shell are energetically preferred for ''Set II.'' This will be discussed in more depth below.

### D. Global and local minimum energy structures

In Fig. 11 we show the global minimum energy structures for the $Xe_nI^-$ clusters with $n = 2–14$ obtained with ''Set II'' (from Table II), including all many-body contributions.[70] In all the clusters the xenon atoms are grouped around the central iodide anion, allowing the maximum number of $Xe–I^-$ bonds to be formed. Each of these is roughly four times stronger than a bond between two xenon atoms. Next, the xenon atoms are grouped in such a way that the number of Xe–Xe bonds is maximized. The $n = 12$ cluster forms an icosahedron of xenon atoms around the central iodide anion. All clusters with $n < 12$ can be seen as fragments derived from this icosahedral structure. Thus, for example, the $n = 6$ cluster represents half an icosahedral shell.

It is convenient to use the following notation to characterize the clusters based on the pictorial representation of Fig. 11. The icosahedron can be referred to as ''1–5–5–1,'' where the first ''1'' denotes the single xenon at the bottom, the ''5'' is the lower five-ring structure, the second ''5'' represents the five atoms of the upper ring structure, and the final ''1'' is the xenon atom at the top. The $n = 6$ ''half-shell'' cluster is termed ''1–5–0–0,'' and an icosahedral cluster with one additional atom in the second solvent shell is labeled ''(1–5–5–1)–1,'' where the parentheses denote a closed first solvent shell.

Interesting effects are observed for $n > 12$. Rather than following the icosahedral motif of $n = 12$, the $n = 13$ cluster is a different closed-shell arrangement (''1–5–6–1''). The lower half still looks very similar to the icosahedron, but a ring of six xenon atoms replaces the upper five-membered

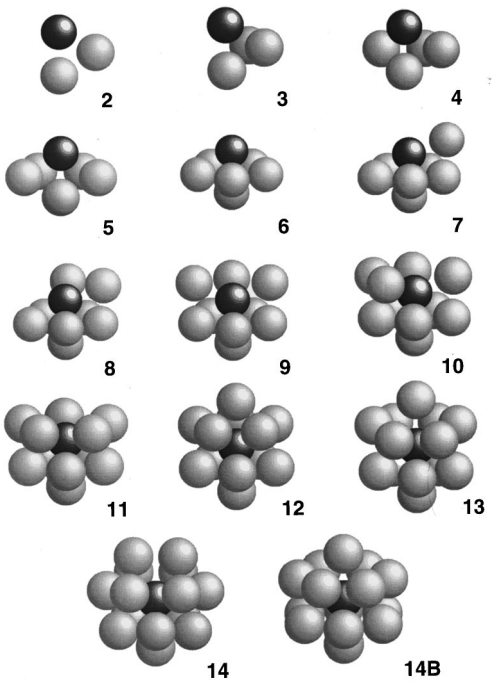


FIG. 11. Global minimum energy structures of $Xe_nI^-$ anion clusters for $n=2-14$. All structures were obtained using the MMSV two-body potential ''Set II'' from Table II, including all many-body options. For $n=14$ two nearly isoenergetic isomers (''14'' and ''14B'') of a different structure exist. Note that ''12,'' ''13,'' ''14,'' and ''14B'' all consist of a closed shell of xenon atoms around the central iodide anion. Xenon and iodide atoms shown with less than their van der Waals radii for the sake of clarity. For details see the text.

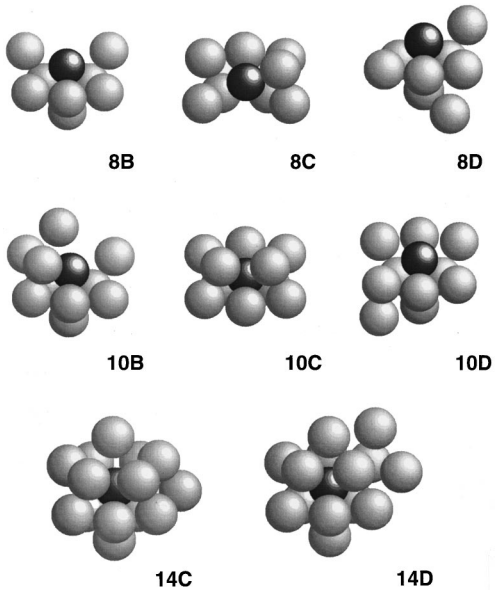


FIG. 12. Selected local minimum energy structures of $Xe_nI^-$ anion clusters for $n=8$, 10, and 14. All structures were obtained using the MMSV two-body potential ''Set II'' from Table II and including all many-body options. Xenon and iodide atoms shown with less than their van der Waals radii for the sake of clarity. For details see the text.

ring structure. Note that the xenon atom at the top can occupy different binding sites on the upper six-membered ring, giving rise to additional isomers that are extremely close in energy to ''13.''

For $n=14$ there are two nearly isoenergetic minimum energy structures of different geometry. Both are again characterized by a closed shell of xenon atoms. The cluster numbered as ''14'' in Fig. 11 can be termed as ''1–5–6–2'' (i.e., compared to the $n=13$ cluster an additional xenon atom is placed on top of the six-ring). This is accompanied by a slight rearrangement of all atoms. The structure can be derived from a decahedron, which has its two halves opened up on the lower side so that the two additional xenon atoms can approach the iodide anion much more closely. The second structure (''14B'') represents a bicapped hexagonal antiprism, and can be described as ''1–6–6–1,'' i.e., now there are two six-rings. As with ''13,'' additional nearly isoenergetic isomers of this structure are possible due to the different binding sites available for the two single xenon atoms at the bottom and top. Note that these two atoms are closer to the central iodide anion than any of the xenon atoms in the six-rings.

The global minimum energy structures for $n=12-14$ obviously all possess a closed shell of xenon atoms, and the question arises as to at what cluster size an additional xenon atom goes into the second solvent shell. We have therefore extended our survey of structures to the clusters with $n=15$ and 16 (not shown here in detail). For $n=15$ a structure very similar to ''14'' in Fig. 11 is obtained, with the additional xenon atom located on top of the six-membered ring. Interestingly, this additional atom is about 0.5 Å farther away from the iodide anion than the next closest xenon atom, so one might think of this cluster as neither fully closed shell (''1–5–6–3'') nor forming a second shell [''(1–5–6–2)–1'']. For $n=16$, however, the crowding becomes so pronounced that the 16th xenon atom is truly located in the second shell: it is almost 1.5 Å farther away than the most distant xenon atom in the $n=15$ cluster. The global minimum energy structure for $n=16$ is based on that of $Xe_{15}I^-$ and might therefore be termed ''(1–5–6–3)–1'' or ''(1–5–6–2)–2.''

The question arises as to how the appearance of almost isoenergetic anion isomers, as, e.g., ''14'' and ''14B,'' affects the trend for our simulated electron affinities. Moreover, the calculated cluster geometries are ''0 K structures,'' whereas the experimental spectra are taken at a finite temperature, so one must consider how the population of local minima could affect our results. We therefore carried out an extensive survey of local minima for all cluster sizes. Selected structures for $n=8$, 10, and 14 can be found in Fig. 12.[70]

In the case of $Xe_8I^-$ the local minimum structures ''8B'' and ''8C'' still have all xenon atoms in contact with the iodide anion (as the global minimum ''8'' in Fig. 11) but fewer Xe–Xe bonds. Including the zero-point energies they are located about 140 and 300 $cm^{-1}$, respectively, above the global minimum. The detachment energies, however, are *almost identical* because the corresponding *X* state structures accessed by photodetachment are destabilized by nearly the same amount. Note also that the $X-I$ and $X-II$ splittings (not shown here) are very similar. The isomer ''8D'' differs from the others as one of the xenon atoms is no longer di-

rectly bound to the iodide anion. This local minimum structure is therefore located at an even higher energy, about 440 $cm^{-1}$ above the global minimum. For this isomer the detachment energy is *260 $cm^{-1}$ lower* than for the lowest-energy isomer.

Very similar results are obtained for the two other examples in Fig. 12 ($n=10$ and 14), as well as for all the other clusters we studied. In nearly all cases, isomers having all xenon atoms in contact with the iodide yield almost identical detachment energies, whereas isomers with less Xe–$I^-$ bonds detach at significantly lower energies (200–260 $cm^{-1}$).

For the interpretation of our ZEKE and PDTP spectra this means the following: Isomers near the global minimum (e.g., ''8''/''8B'' or ''14''/''14B'') will yield almost indistinguishable spectra. In contrast, higher lying isomers should produce features clearly separated in energy. Note that 260 $cm^{-1}$ ($Xe_8I^-$) correspond to about twice the size of the experimental $X-I$ splittings in Fig. 9(a). Most important, *an ''isomer splitting'' of the same size must also appear in the II state spectra; however, such a splitting is not observed in these spectra*. On the contrary—the PDTP spectra show only a single peak and are much narrower than those for the corresponding *X* and *I* states [Fig. 5(c)].

It is also illuminating to consider the shell closing for different potential models in greater detail. As is clear from the discussion above, the structures calculated with ''Set II,'' including all many-body terms, do not show a well-defined shell closing at a single specific *n*; in fact, $n=12-14$ are all clear closed-shell structures. This behavior, together with the specific structure and energetics of the neutral clusters accessed by photodetachment, results in the specific curvature of the electron affinity curve in Fig. 7(a). Moreover, for $n=13$ and 14, structures based on the icosahedral motif cannot compete energetically. In contrast, if pair potentials alone are used, we find that for the $n=13$ cluster the 13th xenon atom goes into the second solvent shell, and this is why the pairwise-additive model yields a sharp drop in slope of the electron affinity at $n=12$.

Finally, we comment on the relation between electron affinities and peak intensities in the $Xe_nI^-$ mass spectrum. Becker *et al.*[28,29] reported a particularly intense ''magic number'' peak for $Xe_{12}I^-$. Here, we found the mass peak intensities to decrease monotonically with cluster size up to $n=12$, and cluster intensities above $n=12$ were considerably lower. Observations of this type are often attributed to shell closing, but a shell closing at $n=12$ in the anion is inconsistent with our electron affinities and simulations.

While mass spectra are sensitive primarily to the relative stablilites of the anions, electron affinities depend on both anion and neutral binding energies. To illustrate this point, we show in Fig. 13 ''sequential solvation energies'' for the $Xe_nI^{(-)}$ anion and neutral clusters, which we calculated from the global minimum energy structures obtained from our MD simulations. The sequential solvation energy $\Delta SE(n)$ of a cluster with *n* xenon atoms is defined as

$$\Delta SE(n)=E_C(n)-E_C(n-1)$$
$$=\epsilon(n)-\omega_0(n)-\epsilon(n-1)+\omega_0(n-1), \qquad (15)$$

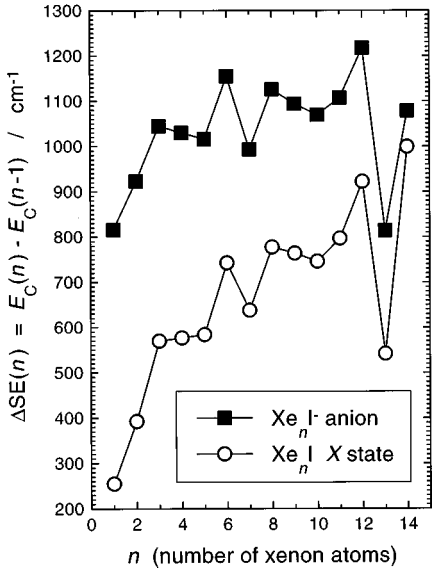


FIG. 13. Sequential solvation energies $\Delta SE(n)=E_C(n)-E_C(n-1)$ [Eq. (15)] as a function of the cluster size. ''■:'' anion clusters; ''○:'' *X* state clusters. All values were obtained using the MMSV two-body potential ''Set II'' from Table II, including all many-body options. The energetic difference in $\Delta SE(n)$ between the anion and *X* state clusters represents the ''sequential electron affinity'' $\Delta EA(n)=EA(n)-EA(n-1)$. For details see the text.

where $E_C(n)$ represents the difference between the well depth $\epsilon(n)$ and the zero-point energy $\omega_0(n)$. The resulting $\Delta SE(n)$ for the anion and *X* state clusters are shown in the plot (''■'' and ''○,'' respectively). Note that the energetic difference in $\Delta SE(n)$ between the anion and *X* state clusters represents the ''sequential electron affinity'' $\Delta EA(n)=EA(n)-EA(n-1)$ [compare Eqs. (3) and (15)].

The shape of the anion and neutral curves in Fig. 13 is very similar. $\Delta SE(n)$ is largest for the anion cluster with $n=12$, and this cluster is therefore particularly stable. This is easy to understand on the basis of the global minimum energy structures already presented in Fig. 11: the addition of the 12th xenon atom to the $n=11$ cluster leads to the formation of one additional Xe–$I^-$ bond and five (nearest neighbor) Xe–Xe bonds. In contrast, at $n=7$ there is a dip in the $\Delta SE(n)$ curves, because in this case only two Xe–Xe bonds are formed in addition to the Xe–$I^-$ bond.

The most interesting feature is the sharp drop in $\Delta SE(n)$ from $n=12$ to $n=13$. The $n=13$ cluster possesses the lowest $\Delta SE$ value of all anion clusters. This decreased stabilization of the $n=13$ anion cluster and the particular stability of the $n=12$ anion cluster is consistent with the peak intensities observed in the mass spectra of $Xe_nI^-$. However, the simulations show that this drop in $\Delta SE(n)$ is *not* due to a shell closing. In addition, this decrease in $\Delta SE(n)$ is about the same for both the anion and neutral and is therefore not apparent from the electron affinity measurements. It therefore appears that one should use caution in inferring shell closings on the basis of mass spectrometry or electron affinity measurements alone.

### E. Effects of excited states in $Xe_nI^-$ clusters

Recently, Cheshnovsky and co-workers obtained total photodetachment cross sections (TPCS) for $Xe_nI^-$ clusters ($n=1-54$).[28,29] Their spectra for $n\geqslant 4$ showed the development of three narrow peaks close to the detachment thresholds for the neutral *X, I,* and *II* states. These were assigned to transitions to excited electronic states in the anion cluster in which the electron is delocalized over the highly polarizable xenon atoms. These electronic excitation energies were found to be less than the vertical detachment energies determined via relatively low resolution (~60 meV) photoelectron spectroscopy of the $Xe_nI^-$ clusters; based on this, these excited states were termed ''bound delocalized excited states.''

The peaks in the TPCS spectra are remarkably similar to those seen in our ZEKE and PDTP spectra. This is at first glance surprising, because peaks in a TPCS experiment should correspond to excited anion states that decay by autodetachment, whereas ZEKE and PDTP experiments measure transitions that generally involve direct photodetachment to neutral vibrational/electronic states. However, there are important differences between the two sets of results which do indicate the two sets of experiments are measuring different phenomena. First, we observe peaks for all $Xe_nI^-$ clusters, not just those with $n\geqslant 4$. Second, for many of the clusters, the peaks in the ZEKE/PDTP experiments occur at slightly higher energy than in the TPCS experiments. For example, the peaks for the $n=4-8$ clusters in Fig. 5(a) (corresponding to the *II* state) are progressively blue-shifted (5–25 meV) relative to the corresponding resonances seen by Becker and Cheshnovsky.[29] For the *X* and *I* states, the peaks in our ZEKE/PDTP experiments also appear at somewhat higher energies than in the TPCS spectra for most of the clusters with $n\leqslant 12$ (e.g., about 5 meV higher for $n=7$). However, for these lower-energy features the differences between the two sets of experiments are definitely smaller than for the peaks corresponding to the *II* states.

This situation bears close comparison with previous work on $C_6^-$, in which a series of peaks in the ZEKE spectrum occurred at 5 meV higher energy than the corresponding peaks in the TPCS measurement.[41] The TPCS peaks were attributed to autodetaching anion excited states lying just below (i.e., 5 meV) the corresponding direct detachment thresholds, as determined in the ZEKE experiment. We believe that a similar explanation holds for the $Xe_nI^-$ clusters, although the situation is somewhat less clear because the peaks are much broader than for $C_6^-$ and, in most cases, overlap in the two sets of experiments.

The question remains as to how the presence of the anion excited states affects the ZEKE/PDTP experiments. The overlap of the peaks in the two sets of experiments means that resonant excitation to the excited anion state as well as direct photodetachment contribute to the absorption cross section near each photodetachment threshold. We do observe that the intensities of the ZEKE and PDTP signals increase markedly with cluster size, which could certainly result from an increasingly strong resonant contribution to the cross section. However, we have no reason to believe that the peak positions in our experiments are affected by the presence of anion excited states.

## VI. CONCLUSIONS

ZEKE and PDTP spectroscopy of the $Xe_nI^-$ anion clusters with $n=2-14$ has allowed us to determine adiabatic electron affinities and splittings between the neutral electronic states accessed by photodetachment. Clear double peak structures in the ZEKE spectra for $n=2-12$ could be unambiguously assigned as bands arising from transitions to the neutral *X* and *I* states. In contrast, the *II* state band for each cluster in the PDTP spectra for $n=2-8$ is much narrower and shows no splitting.

With the help of simulated annealing MD calculations of the cluster structures we could show that EAs calculated from pair potentials alone (i.e., without any nonadditive effect included) drastically overestimate the experimental values. The dominant many-body effect is nonadditive induction, specifically the *repulsion* between the charge-induced dipoles on adjacent xenon atoms. This effect alone accounts for most of the discrepancy between ''additive'' and experimental EAs, but definitely overcorrects.

Inclusion of the *attractive* charge-exchange quadrupole term provides the main contribution that counteracts this overcorrection and brings the calculated EAs even closer to experiment. However, the Gaussian range parameter for the $Xe_2$ exchange quadrupole is not extremely well defined (see the Appendix). Therefore, although we obtained optimal agreement with the experimental EAs by additionally including the charge-dispersion multipole and Axilrod–Teller triple-dipole terms in our simulations, one should be careful with conclusions about the exact influence of the latter two effects, as we have also neglected three-body exchange and higher-order multipole dispersion terms, as, e.g., dipole–dipole–quadrupole. On the other hand, these effects are operative in both the anion and neutral clusters and should at least partially cancel out as far as the electron affinities are concerned.

Qualitatively, our findings about the relative importance of the individual many-body effects agree very well with our earlier results for the $Ar_nI$ and $Ar_nBr$ systems.[39] However, the absolute magnitude of the many-body effects for $Xe_nI^-$ is much larger due to the much higher polarizability of xenon relative to argon.

The $Xe_nI^-$ anion global minimum structures obtained from the simulated annealing MD calculations show interesting trends. The clusters $Xe_{12}I^-$, $Xe_{13}I^-$, and $Xe_{14}I^-$ all form a closed shell of xenon atoms around the iodide anion. These specific structures are also a direct consequence of many-body effects. In contrast, pure pair potentials predict a shell closing at $n=12$, and in this case the additional xenon atom for $n=13$ would be attached to the outside of the first solvent shell.

The specific dependence of the experimental EAs on cluster size also allowed us to refine the absolute $Xe–I^{(-)}$ bond lengths for the anion, *X, I,* and *II* state diatomic potentials to within $\pm 0.05$ Å without changing the relative positions of the potential curves or their shape in the Franck–Condon region (relative to our original potential set).[33]

## ACKNOWLEDGMENTS

This research is supported by the Air Force Office of Scientific Research under Grant No. F49620-97-1-0018. T. Lenzer is grateful to the Deutsche Forschungsgemeinschaft for a postdoctoral fellowship, and M. R. Furlanetto thanks the National Science Foundation for a predoctoral fellowship. We thank J. Troe for providing most of the computer time needed for the simulated annealing calculations, I. Yourshaw, R. B. Gerber, P. Jungwirth, A. Krylov, C. C. Martens, and Z. Li for providing early versions of the molecular dynamics programs, and N. J. Wright for useful discussions and a copy of Ref. 71. We also thank O. Cheshnovsky for providing results prior to publication.


## APPENDIX: MANY-BODY EFFECTS

The most important equations for describing the various many-body effects included in the simulations (Sec. IV B) are summarized in the following. For additional details see our earlier publication.[39]

### 1. Nonadditive induction

We calculate the nonadditive induction term within the framework of the ''full iteratively calculated induction model.'' [39] The total induction energy of a $Xe_nI^-$ anion cluster is given by

$$V_{1,\mathrm{total}}=\frac{1}{2}(V_{q\mu}+V_{q\Theta})$$

$$=\sum_i \sum_{j\neq i} q_i\left(-\frac{1}{2}T_{\alpha}^{(ij)}\mu_{\alpha}^{(j)}+\frac{1}{6}T_{\alpha\beta}^{(ij)}\Theta_{\alpha\beta}^{(j)}\right). \quad \text{(A1)}$$

Following Buckingham,[72] the subscripts $\alpha$ and $\beta$ denote any of the Cartesian components of a vector or tensor, and repeated Greek subscripts stand for summation over the three components. $q_i$ is the permanent electric charge of atom $i$ ($-1$ for iodide and 0 for xenon). $\mu_{\alpha}^{(i)}$ and $\Theta_{\alpha\beta}^{(i)}$ are components of the induced dipole and quadrupole moments, respectively, at atom $i$, given by[72]

$$\mu_{\alpha}^{(i)}=\alpha_i E_{\alpha}^{(i)} \quad \text{(A2)}$$

and

$$\Theta_{\alpha\beta}^{(i)}=C_i E_{\alpha\beta}^{(i)}. \quad \text{(A3)}$$

The values for the dipole and quadrupole polarizabilities $\alpha$ and $C$ used in this work are given in Table III (note that $\alpha=\alpha_d$). The multipole tensors are defined as

$$T_{\alpha\beta}^{(ij)}=\nabla_{\alpha}\nabla_{\beta}(1/R_{ij}), \quad \text{(A4)}$$

where $\mathbf{R}_{ij}$ is the vector from atom $j$ to atom $i$. $E_{\alpha}^{(i)}$ represents the electric field at atom $i$,[77]

$$E_{\alpha}^{(i)}=\sum_{j\neq i}\left(-T_{\alpha}^{(ij)}q_j+T_{\alpha\beta}^{(ij)}\mu_{\beta}^{(j)}-\frac{1}{3}T_{\alpha\beta\gamma}^{(ij)}\Theta_{\beta\gamma}^{(j)}\right), \quad \text{(A5)}$$

and the electric field gradient $E_{\alpha\beta}^{(i)}$ is then given by[72]

$$E_{\alpha\beta}^{(i)}=\sum_{j\neq i}\left(-T_{\alpha\beta}^{(ij)}q_j+T_{\alpha\beta\gamma}^{(ij)}\mu_{\gamma}^{(j)}-\frac{1}{3}T_{\alpha\beta\gamma\delta}^{(ij)}\Theta_{\gamma\delta}^{(j)}\right). \quad \text{(A6)}$$

TABLE III. Atomic dipole and quadrupole polarizabilities, the effective number of electrons, and triple-dipole $C_9$ coefficients for Xe–Xe–$I^-$ and Xe–Xe–I interactions. Values for the quadrupole polarizabilities $C$ are based on Buckingham's definition ($C=0.5\cdot\alpha_q$) (Ref. 72).

| Atom | $\alpha_d$ ($a_0^3$) | $C$ ($a_0^5$) | $N$ | $C_9$ [eV Å$^9$] |
|---|---|---|---|---|
| Xe | 27.16[a] | 101.4[b] | 7.253[c] | --- |
| $I^-$ | 52.7[d] | 254[e] | 7.253[c] | 882 |
| I | 33.1[f] | --- | 6.5[f] | 595 |

[a]Reference 73.
[b]Reference 74.
[c]Calculated from the $C_6$ value of Ref. 73.
[d]Reference 75.
[e]Reference 76.
[f]Reference 77.

We use Buckingham's definition of the quadrupole moment as a traceless tensor.[72] Equation (A1) already explicitly includes the Xe–I pair potential. To extract the additive portion $V_{\mathrm{I,p}}$ of $V_{\mathrm{I,total}}$, the induction energy for each Xe–I pair is calculated neglecting the other xenon atoms in the cluster using the above equations. Finally, the nonadditive induction energy $V_I$ is obtained via

$$V_{\mathrm{I}}=V_{\mathrm{I,total}}-V_{\mathrm{I,p}}. \quad \text{(A7)}$$

### 2. Charge–exchange quadrupole interaction

To model this effect we use the ''Gaussian exchange charge'' formalism.[39] For calculating the interaction energy between the iodide charge and the exchange quadrupole an effective charge density $\rho_{\mathrm{eff}}$ is formed, which gives the part of the charge density that contributes to the exchange quadrupole:

$$\rho_{\mathrm{eff}}(r)=-|e|\int|\Psi_{ij}^0(\mathbf{r},\mathbf{r}')|^2d\mathbf{r}'-\rho_i(\mathbf{r})-\rho_j(\mathbf{r})$$

$$=-\frac{|e|S_{ij}^2}{1-S_{ij}^2}\left(\frac{\beta}{\sqrt{\pi}}\right)^3$$

$$\times[e^{-\beta^2|\mathbf{R}_i-\mathbf{r}|^2}+e^{-\beta^2|\mathbf{R}_j-\mathbf{r}|^2}-2e^{-\beta^2|\mathbf{R}_c-\mathbf{r}|^2}]. \quad \text{(A8)}$$

Here $\mathbf{R_c}$ represents the midpoint between the two xenon nuclei [$\mathbf{R_c}=0.5(\mathbf{R}_i+\mathbf{R}_j)$]. $\rho_{\mathrm{eff}}$ is made up from two negative Gaussian charge distributions located at the xenon nuclei, and a positive Gaussian charge distribution, twice as large, at $\mathbf{R_c}$.[64] If one approximates the iodide with a point charge at $\mathbf{R_0}$, the Coulomb interaction energy $V_{\mathrm{C-E}}$ between the charge and the exchange quadrupole is given by[78,79]

$$V_{\mathrm{C-E}}=\sum_{i<j}\frac{e^2S_{ij}^2}{1-S_{ij}^2}\left(\frac{\mathrm{erf}(\beta R_{i0})}{R_{i0}}+\frac{\mathrm{erf}(\beta R_{j0})}{R_{j0}}-2\frac{\mathrm{erf}(\beta R_{\mathrm{C0}})}{R_{\mathrm{C0}}}\right). \quad \text{(A9)}$$

$R_{i0}$, $R_{j0}$, and $R_{\mathrm{C0}}$ are the distances of the iodide from the xenon nuclei and the midpoint between the nuclei, respectively; $i$ and $j$ run over the xenon atoms, and $\beta$ is the Gaussian range parameter of the electron density. Nonphysical be-

havior of Eq. (A9) for small $R_{C0}$ values (near linear geometries) is prevented by cutting off $V_{C-E}$ for Xe–Xe separations greater than typically 6.5 Å.

This ''Gaussian exchange charge'' model requires an estimate for the $\beta$ parameter of xenon. The only value available comes from Jansen's work [$\beta(\mathrm{Xe})=0.454\,\text{Å}^{-1}$],[80] however, his values are known to underestimate the real ones severely:[81,82] as an example, in the case of $Ar_2$ Jansen recommends $\beta(\mathrm{Ar})=0.632\,\text{Å}^{-1}$. This can be compared with the values 0.936[20] and 0.965 $\text{Å}^{-1}$ [16] that were extracted by Hutson and co-workers from a SCF calculation and distributed multipole analysis of the $Ar_2$ quadrupole moment,[71] or with $\beta(\mathrm{Ar})=1.08\,\text{Å}^{-1}$, as recommended by Guillot *et al.*[81]

A better, but probably still too low, estimate for xenon can be obtained, e.g., by rescaling Jansen's $\beta$(Xe) by the ratio $\beta$(Ar,Hutson)/$\beta$(Ar,Jansen). By this we arrive at roughly 0.7 $\text{Å}^{-1}$. For $Kr_2$, Guillot *et al.*[81] recommend a value of 0.84 $\text{Å}^{-1}$, which certainly overestimates the xenon value. In this study we used $\beta(\mathrm{Xe})=0.765\,\text{Å}^{-1}$ as a reasonable estimate, which also gave the best agreement with our experimental electron affinities, especially for $Xe_2I^-$.

### 3. Charge-dispersion multipole interactions

Following Hunt[65] the average dipole moment induced on atom *i* by the dispersion interaction with other like atoms is given by

$$\mu^{i,\mathrm{disp}}=C_\mu\sum_{j\neq i}\frac{\hat{\mathbf{R}}_{ij}}{R_{ij}^7},\quad \text{with}\quad C_\mu=\frac{3C_6B}{2\alpha}. \tag{A10}$$

Here, $\hat{\mathbf{R}}_{ij}$ denotes the unit vector pointing from atom *j* to *i*, $\alpha$ is the xenon dipole polarizability (Table III), $C_6$ is the Xe–Xe dispersion coefficient, and *B* represents the xenon dipole–quadrupole hyperpolarizability.

The components of the dispersion-induced quadrupole moment on atom *i* are calculated via

$$\Theta_{\alpha\beta}^{i,\mathrm{disp}}=-C_\Theta\sum_{j\neq i}\frac{T_{\alpha\beta}^{(ij)}}{2R_{ij}^3},\quad \text{with}\quad C_\Theta=\frac{C_6B}{4\alpha}, \tag{A11}$$

with the quadrupole tensor defined as in Eq. (A4). $C_6$ was taken from the Xe–Xe HFD-B2 potential of Aziz, Meath, and co-workers ($C_6=283.9e^2a_0^5$).[53] To our knowledge there is no experimental information on *B*, and the only value available so far comes from DFT calculations of Senatore and Subbaswamy.[83] The hyperpolarizabilities from this study are expected to be too large in absolute value.[83,84] We have therefore rescaled their xenon value ($B=-912a_0^6/e$) by the ratio of the experimental and DFT *cubic* hyperpolarizabilities $\gamma_{\mathrm{exp}}(\mathrm{Xe})/\gamma_{\mathrm{DFT}}(\mathrm{Xe})=0.825$,[78,79] yielding a value of $B=-752a_0^6/e$. Note that a similar procedure works extremely well in the case of argon, where the rescaled value is $B=-155a_0^6/e$ compared to $-141a_0^6/e$ and $-164.3a_0^6/e$ obtained in two other theoretical studies.[85,86]

The total dispersion induced dipoles and quadrupoles can then be calculated via Eqs. (A10) and (A11) for each xenon atom. Finally, standard electrostatic formulas are used to evaluate the charge–dipole and the charge–quadrupole interaction energies, $V_{C-D}$ and $V_{C-Q}$, respectively.[72]

### 4. Axilrod–Teller triple–dipole interaction

The leading term in the nonadditive dispersion energy, the triple-dipole interaction is given by[66–68]

$$V_A=C_9\frac{(3\cos\theta_i\cos\theta_j\cos\theta_k+1)}{R_{ij}^3R_{jk}^3R_{ik}^3}, \tag{A12}$$

with $\theta_i$ being the interior angle $\angle jik$, $R_{ij}$ represents the internuclear distance between atoms *i* and *j*, and $C_9$ is the triple-dipole coefficient that depends on the type of atoms involved. $C_9$ coefficients are now available for a variety of systems,[87–90] but unfortunately not for the interactions (Xe–Xe–I and Xe–Xe–I) relevant to this paper. Therefore, we use the following approximation for $C_9$:[39,89,91–93]

$$C_9=\frac{3}{2}\alpha_i\alpha_j\alpha_k\frac{\eta_i\eta_j\eta_k(\eta_i+\eta_j+\eta_k)}{(\eta_i+\eta_j)(\eta_j+\eta_k)(\eta_i+\eta_k)}. \tag{A13}$$

Here $\alpha_i$ and $\eta_i$ are the dipole polarizability and the average excitation energy of atom *i*, respectively. $\eta_i$ (in a.u.) can be approximated as[91–96]

$$\eta_i=\sqrt{N_i/\alpha_i}, \tag{A14}$$

where $N_i$ is an effective number of electrons depending on the type of atom involved. Values for $\alpha$ and *N* can be found in Table III (note again that $\alpha=\alpha_d$).


[1] P. K. Walhout, J. C. Alfano, K. A. M. Thakur, and P. F. Barbara, J. Phys. Chem. **99**, 7568 (1995).
[2] T. Kühne, R. Küster, and P. Vöhringer, Chem. Phys. **233**, 161 (1998).
[3] M. E. Fajardo and V. A. Apkarian, J. Chem. Phys. **89**, 4102 (1988).
[4] W. G. Lawrence and V. A. Apkarian, J. Chem. Phys. **101**, 1820 (1994).
[5] J. M. Papanikolas, J. R. Gord, N. E. Levinger, D. Ray, V. Vorsa, and W. C. Lineberger, J. Phys. Chem. **95**, 8028 (1991).
[6] S. Nandi, A. Sanov, N. Delaney, J. Faeder, R. Parson, and W. C. Lineberger, J. Phys. Chem. A **102**, 8827 (1998).
[7] B. J. Greenblatt, M. T. Zanni, and D. M. Neumark, Faraday Discuss. **108**, 101 (1997).
[8] B. J. Greenblatt, M. T. Zanni, and D. M. Neumark, Science **276**, 1675 (1997).
[9] H. Margenau and N. R. Kestner, *Theory of Intermolecular Forces* (Pergamon, Oxford, 1969).
[10] M. J. Elrod and R. J. Saykally, Chem. Rev. **94**, 1975 (1994).
[11] Z. Bacic and R. E. Miller, J. Phys. Chem. **100**, 12 945 (1996).
[12] Y. Xu, W. Jäger, and M. C. L. Gerry, J. Chem. Phys. **100**, 4171 (1994).
[13] M. J. Elrod, J. G. Loeser, and R. J. Saykally, J. Chem. Phys. **98**, 5352 (1993).
[14] M. M. Szczesniak, G. Chalasinski, and P. Piecuch, J. Chem. Phys. **99**, 6732 (1993).
[15] S. M. Cybulski, M. M. Szczesniak, and G. Chalasinski, J. Chem. Phys. **101**, 10 708 (1994).
[16] A. R. Cooper and J. M. Hutson, J. Chem. Phys. **98**, 5337 (1993).
[17] M. A. Suhm and D. J. Nesbitt, Chem. Soc. Rev. **24**, 45 (1995).
[18] A. McIlroy, R. Lascola, C. M. Lovejoy, and D. J. Nesbitt, J. Phys. Chem. **95**, 2636 (1991).
[19] C.-C. Chuang, S. N. Tsang, J. G. Hanson, W. Klemperer, and H.-C. Chang, J. Chem. Phys. **107**, 7041 (1997).
[20] A. Ernesti and J. M. Hutson, Phys. Rev. A **51**, 239 (1995).
[21] V. F. Lotrich, P. Jankowski, and K. Szalewicz, J. Chem. Phys. **108**, 4725 (1998).
[22] M. J. Elrod, R. J. Saykally, A. R. Cooper, and J. M. Hutson, Mol. Phys. **81**, 579 (1994).
[23] J. M. Sperhac, M. J. Weida, and D. J. Nesbitt, J. Chem. Phys. **104**, 2202 (1996).
[24] J. Rak, M. M. Szczesniak, G. Chalasinski, and S. M. Cybulski, J. Chem. Phys. **106**, 10 215 (1997).
[25] J. P. Visticot, P. de Pujo, J. M. Mestdagh, A. Lallement, J. Berlande, O. Sublemontier, P. Meynadier, and J. Cuvellier, J. Chem. Phys. **100**, 158 (1994).

[26] S. Martrenchard-Barra, C. Jouvet, C. Lardeux-Dedonder, and D. Solgadi, J. Chem. Phys. **98**, 5281 (1993).
[27] G. Markovich, S. Pollack, R. Giniger, and O. Cheshnovsky, J. Chem. Phys. **101**, 9344 (1994).
[28] I. Becker, G. Markovich, and O. Cheshnovsky, Phys. Rev. Lett. **79**, 3391 (1997).
[29] I. Becker and O. Cheshnovsky, J. Chem. Phys. (in press).
[30] S. T. Arnold, J. H. Hendricks, and K. H. Bowen, J. Chem. Phys. **102**, 39 (1995).
[31] D. W. Arnold, S. E. Bradforth, E. H. Kim, and D. M. Neumark, J. Chem. Phys. **102**, 3510 (1995).
[32] D. W. Arnold, S. E. Bradforth, E. H. Kim, and D. M. Neumark, J. Chem. Phys. **97**, 9468 (1992).
[33] T. Lenzer, M. R. Furlanetto, K. R. Asmis, and D. M. Neumark, J. Chem. Phys. **109**, 10 754 (1998).
[34] L. S. Sremaniak, L. Perera, and M. L. Berkowitz, Chem. Phys. Lett. **218**, 377 (1994).
[35] L. X. Dang and B. C. Garrett, J. Chem. Phys. **99**, 2972 (1993).
[36] I.-C. Yeh, L. Perera, and M. L. Berkowitz, Chem. Phys. Lett. **264**, 31 (1997).
[37] I. Yourshaw, T. Lenzer, G. Reiser, and D. M. Neumark, J. Chem. Phys. **109**, 5247 (1998).
[38] Y. Zhao, I. Yourshaw, G. Reiser, C. C. Arnold, and D. M. Neumark, J. Chem. Phys. **101**, 6538 (1994).
[39] I. Yourshaw, Y. Zhao, and D. M. Neumark, J. Chem. Phys. **105**, 351 (1996).
[40] T. N. Kitsopoulos, I. M. Waller, J. G. Loeser, and D. M. Neumark, Chem. Phys. Lett. **159**, 300 (1989).
[41] C. C. Arnold, Y. Zhao, T. N. Kitsopoulos, and D. M. Neumark, J. Chem. Phys. **97**, 6121 (1992).
[42] T. N. Kitsopoulos, Ph.D. thesis, University of California, Berkeley, 1991.
[43] C. C. Arnold, Ph.D. thesis, University of California, Berkeley, 1994.
[44] T. Baer, W. B. Peatman, and E. W. Schlag, Chem. Phys. Lett. **4**, 243 (1969).
[45] R. Spohr, P. M. Guyon, W. A. Chupka, and J. Berkowitz, Rev. Sci. Instrum. **42**, 1872 (1971).
[46] T.-K. Ha, Y. He, J. Pochert, M. Quack, R. Ranz, G. Seyfang, and I. Thanopoulos, Ber. Bunsenges. Phys. Chem. **99**, 384 (1995).
[47] Handbook of Chemistry and Physics, 77th ed. (CRC Press, Boca Raton, 1996).
[48] ORIGIN 5.0, Microcal Software Inc., Northampton, MA 01060, 1997.
[49] D. Hanstorp and M. Gustafsson, J. Phys. B **25**, 1773 (1992).
[50] D. T. Radzykewycz and J. Tellinghuisen, J. Chem. Phys. **105**, 1330 (1996).
[51] P. Casavecchia, G. He, R. K. Sparks, and Y. T. Lee, J. Chem. Phys. **77**, 1878 (1982).
[52] D. Schröder, J. N. Harvey, M. Aschi, and H. Schwarz, J. Chem. Phys. **108**, 8446 (1998).
[53] A. K. Dham, W. J. Meath, A. R. Allnatt, R. A. Aziz, and M. J. Slaman, Chem. Phys. **142**, 173 (1990).
[54] W. E. Baylis, J. Phys. B **10**, L477 (1977).
[55] D. L. Huestis and N. E. Schlotter, J. Chem. Phys. **69**, 3100 (1978).
[56] F. O. Ellison, J. Am. Chem. Soc. **85**, 3540 (1963).
[57] J. C. Tully, J. Chem. Phys. **58**, 1396 (1972).
[58] K. M. Sando, G. J. Erickson, and R. C. Binning, Jr., J. Phys. B **12**, 2697 (1979).
[59] G. J. Erickson and K. M. Sando, Phys. Rev. A **22**, 1500 (1980).
[60] H. Haberland, Z. Phys. A **307**, 35 (1982).
[61] V. Aquilanti, G. Liuti, F. Pirani, and F. Vecchiocattivi, J. Chem. Soc., Faraday Trans. 2 **85**, 955 (1989).
[62] V. Aquilanti and G. Grossi, J. Chem. Phys. **73**, 1165 (1980).
[63] R. L. Asher, D. A. Micha, and P. J. Brucat, J. Chem. Phys. **96**, 7683 (1992).
[64] B. G. Dick, Jr. and A. W. Overhauser, Phys. Rev. **112**, 90 (1958).
[65] K. L. C. Hunt, Chem. Phys. Lett. **70**, 336 (1980).
[66] B. M. Axilrod and E. Teller, J. Chem. Phys. **11**, 299 (1943).
[67] B. M. Axilrod, J. Chem. Phys. **19**, 719 (1951).
[68] Y. Muto, Proc. Phys. Math. Soc. Jpn. **17**, 629 (1943).
[69] P. J. M. van Laarhoven and E. H. L. Aarts, *Simulated Annealing: Theory and Applications* (Reidel, Dordrecht, 1987).
[70] RASMOL 2.6B2 Molecular Graphics Visualisation Tool, Roger Sayle, Biomolecular Structures Group, Glaxo Wellcome Research & Development, Stevenage, Hertfordshire, UK, 1996.
[71] A. R. Cooper, Ph.D. thesis, Durham University, 1992.
[72] A. D. Buckingham, Adv. Chem. Phys. **12**, 107 (1967).
[73] A. Kumar and W. J. Meath, Mol. Phys. **54**, 823 (1985).
[74] C. Hättig and B. A. Heß, J. Phys. Chem. **100**, 6243 (1996).
[75] H. Coker, J. Phys. Chem. **80**, 2078 (1976).
[76] M. V. K. Sastri, P. L. Narasimhulu, and K. D. Sen, J. Chem. Phys. **80**, 584 (1984).
[77] E. A. Mason and E. W. McDaniel, Transport Properties of Ions in Gases (Wiley, New York, 1988).
[78] R. J. Wheatley, Mol. Phys. **79**, 597 (1993).
[79] R. J. Wheatley and J. B. O. Mitchell, J. Comput. Chem. **15**, 1187 (1994).
[80] L. Jansen, Adv. Quantum Chem. **2**, 119 (1965).
[81] B. Guillot, R. D. Mountain, and G. Birnbaum, Mol. Phys. **64**, 747 (1988).
[82] W. Kolos and A. Les, Int. J. Quantum Chem. **6**, 1101 (1972).
[83] G. Senatore and K. R. Subbaswamy, Phys. Rev. A **34**, 3619 (1986).
[84] D. P. Shelton and J. E. Rice, Chem. Rev. **94**, 3 (1994).
[85] G. Maroulis and D. M. Bishop, J. Phys. B **18**, 4675 (1985).
[86] I. Cernusak, G. H. F. Diercksen, and A. J. Sadlej, Chem. Phys. Lett. **128**, 18 (1986).
[87] S. A. C. McDowell and W. J. Meath, Mol. Phys. **90**, 713 (1997).
[88] S. A. C. McDowell, A. Kumar, and W. J. Meath, Can. J. Chem. **74**, 1180 (1996).
[89] D. J. Margoliash, T. R. Proctor, G. D. Zeiss, and W. J. Meath, Mol. Phys. **35**, 747 (1978).
[90] X. Li and K. L. C. Hunt, J. Chem. Phys. **107**, 4133 (1997).
[91] A. D. Koutselos and E. A. Mason, J. Chem. Phys. **85**, 2154 (1986).
[92] H. L. Kramer and D. R. Herschbach, J. Chem. Phys. **53**, 2792 (1970).
[93] K. T. Tang, Phys. Rev. **177**, 108 (1969).
[94] J. C. Slater and J. G. Kirkwood, Phys. Rev. **37**, 682 (1931).
[95] K. S. Pitzer, Adv. Chem. Phys. **2**, 59 (1959).
[96] J. N. Wilson, J. Chem. Phys. **43**, 2564 (1965).